Typhoons reseal mountain groundwater systems after earthquake damage

Peter Makus[1*], Nicolas Brantut[2], Luc Illien[1],
Jens M. Turowski[1], Wei-An Chao[3], Jui-Ming Chang[3],
Wen-Yen Chang[4], Wen-Sheng Chen[5], Niels Hovius[1,6]

[1]Section 4.6: Geomorphology, GFZ Helmholtz Centre for Geosciences, Potsdam, Germany.

[2]Section 4.2: Geomechanics and Scientific Drilling, GFZ Helmholtz Centre for Geosciences, Potsdam, Germany.

[3]Department of Civil Engineering, National Yang Ming Chiao Tung University, Hsinchu, Taiwan.

[4]College of Environmental Studies and Oceanography, National Dong Hwa University, Shoufeng, Hualien, Taiwan.

[5]Center for General Education, National Dong Hwa University, Shoufeng, Hualien, Taiwan.

[6]Institute for Earth and Environmental Sciences, University of Potsdam, Potsdam, Germany.

[*]Corresponding author. Email: makus@gfz.de

Short title: Typhoons reseal quake-damaged groundwater systems

Bedrock groundwater supplies water services to half the global population. Earthquakes can disrupt this resource for years by changing subsurface permeability. Several mechanisms have been proposed for these changes, but their influence remains debated, because hydrological observations alone cannot distinguish them. We combine groundwater-derived permeability with seismic wavespeed, a measure of the rock's mechanical state, in Taiwan before and after the 2024 magnitude 7.2 Hualien earthquake. This combination reveals two opposing earthquake effects on mountain groundwater systems. First, shaking modified fracture geometry, increasing permeability, which recovered on the same trajectory as

the seismic wavespeed. Second, months later, two typhoons halved permeability without affecting the rock, whereas earlier typhoons had no effect. We attribute this previously unknown, delayed response to clogging of the seismically opened fracture network with sediment injected by overland flow. Beyond their direct, transient effect, large earthquakes can thus prime mountain groundwater systems for lasting, storm-triggered disruption.

Introduction

Bedrock groundwater is the largest terrestrial freshwater reservoir (*1*), providing drinking water to ~50 % of the global population (*2*). Perturbations to this system can have dramatic socioeconomic and ecological consequences (*3*) and may alter landscape dynamics, for example by impacting landslide distributions (*4*). Among these, earthquake-driven perturbations have been observed for thousands of years (*5*). They manifest, for example, as sudden changes in river discharge (*6*), the appearance or disappearance of springs (*7*), or abrupt changes in water composition (*8*). At depth, groundwater disturbances occur as abrupt recharge or discharge events that can cause excess discharge on the order of cubic kilometres (*9*) or in the form of longer-lasting changes in recharge and drainage dynamics (*10*) with potentially important consequences for fresh water resources. Such perturbations have been attributed to changes in aquifer permeability (*11*). Previous studies have invoked a variety of mechanisms for coseismic permeability changes, such as static strain changes (*12*), the sudden contraction of material leading to increased pore pressure (*13*), comparable to liquefaction, modifications in aquifer confinement (*14, 15*), or the clearing and clogging of pore spaces and fractures (*16*). However, field observations of the mechanisms are lacking, and their importance remains debated. This results in significant uncertainty about postseismic trajectories of mountain groundwater resources.

Tidal transmissivity monitoring (*17*) has been useful in identifying coseismic permeability changes. It is, however, unable to distinguish between the mechanisms causing the change. For example, the commonly invoked clearing and clogging cannot be distinguished from changes in the mechanical state of the rock matrix itself, including the geometry of the fracture network. Independently, various studies have observed coseismic disturbances followed by multi-annual

recovery in the elastic properties of the rock substrate (*18–20*) and in the groundwater system (*11, 21, 22*). Yet we do not know whether substrate and permeability changes respond to earthquakes separately, or in a coupled fashion. This gap makes groundwater recovery times difficult to predict and leaves open whether postseismic events can compound the coseismic disturbance. It can be addressed through a joint study of the two components.

Here, we investigate the co-evolution of the permeability of mountain groundwater systems and substrate properties in response to two large earthquakes to evaluate their coupling. Specifically, we compare the time-dependent transmissivity (*23*), which is proportional to the permeability of the groundwater network, with changes in the seismic wavespeed (*24*) that depend on rock stiffness. Independent observables enable us to distinguish mechanisms associated with substrate changes, such as spatially distributed fracture opening, which would manifest in both records simultaneously, from mechanisms confined to the groundwater system, such as fracture clearing or clogging, which affect transmissivity only.

We pursue this comparison with seismological and hydrometric data from the Liwu River catchment in the east flank of the Taiwan Central Range (see Fig. 1). Taiwan is located above a system of subduction zones that cause regular large earthquakes and produce steep mountain topography with fast sediment generation. Furthermore, Taiwan experiences regular typhoons, causing intense rainfall and flooding that can quickly transfer large amounts of sediment. Regional aquifers are hosted by a body of bedrock with a deeply penetrating network of fractures. Locally, the degree of fracturing varies substantially — low transmissivity portions constitute aquitards. This bedrock is overlain by an irregular high-transmissivity layer of regolith and colluvium (*25*). In April 2024, an M7.2 megathrust earthquake occurred just off the coast of Hualien at a depth of ~35 km and about 40 km south of the Liwu catchment. The Hualien earthquake is the largest seismic event recorded around Taiwan in the last quarter century, causing thousands of coseismic landslides (*26*) and perturbing the fractured bedrock aquifers of the eastern Central Range along with its surface hydrological system. Four and seven months later, the typhoons Gaemi and Kong-Rey impacted the earthquake's epicentral area. The latter was one of Taiwan's most intense typhoons in recent history (*27*) with more than 1000 mm of precipitation at our field site. We probe the effects of this distinct combination of events on the groundwater system and the bulk substrate by leveraging recordings from a dense network of groundwater wells and seismic stations. From our analysis,

we infer two opposing effects on the permeability of the groundwater network: first, coseismic permeability increases associated with bulk substrate changes and, second, typhoon-induced but earthquake-primed clogging causing sudden permeability decreases.

Results

The impact of extreme weather and earthquakes on the raw water level

Groundwater data from four boreholes show typhoon-induced and coseismic changes (see Fig. 2), illustrating the range of drainage dynamics. Outside such events, the piezometric levels follow a common annual cycle. Typhoons and other extreme rain events lead to spikes followed by enhanced drainage. For EH-04 and EHW-01, these spikes occurred with almost no delay, and drainage is fast. In contrast, EHW-03 and EHW-02 reach their maxima with a delay relative to the rainfall and drain more slowly.

Earthquakes can interrupt this pattern. Prior to the M7.2 Hualien earthquake, the water levels in all four wells were gradually decreasing as part of the common annual cycle. All wells recorded a sudden step rise of 1–3.5 m coincident with the earthquake, followed by a decay on the order of 6 hours in all wells except in EHW-03. In the following months, two wells — EHW-03 and EH-04 — returned to their pre-earthquake declining trend, whereas the trend steepened for EHW-01 and EHW-02 compared to before the earthquake. More subtle groundwater changes occurred in these four wells after the 2022 M6.5 and M6.9 Taitung earthquake sequence, which struck ~100 km south of the Liwu catchment at a shallow depth of around 10 km.

Time-dependent transmissivity

We obtain the time-dependent transmissivity from July 2021 to November 2025 by fitting the 10-minute-sampled semidiurnal tidal response in the piezometric head to the solid Earth tides and barometric fluctuations. This analysis yields time-dependent transfer functions that we invert for the transmissivity, assuming a leaky-aquifer model (see Materials and Methods for details). Independent pump tests, performed in 2013 for depth ranges between 5 and 100 m within the wells (see table S1), provide a reference order of magnitude for the transmissivity. Of the four

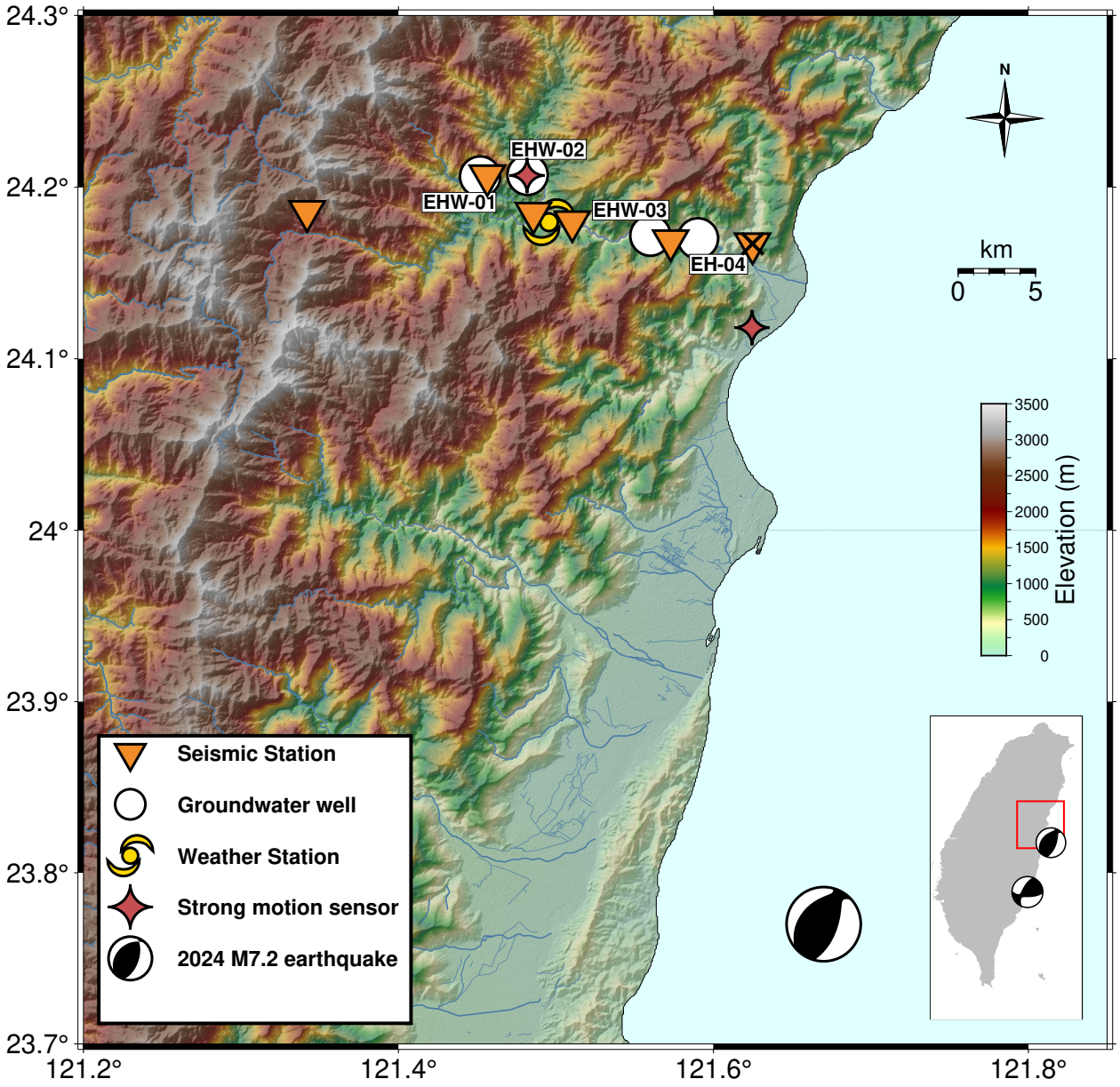


Figure 1: **Locations of sensors, from which data were used.** Data from the seismic station marked with a cross (TQ01) have been used to produce Fig. 3. We used data from well EHW-02 co-located with the strong motion sensor F072 to perform the tidal analysis. The remaining three wells were used only for the groundwater compensation of $\delta v/v$. The map inset contains the moment tensor solutions for the M7.2 2024 Hualien and M6.9 2022 Taitung (outside the map limits) earthquakes.

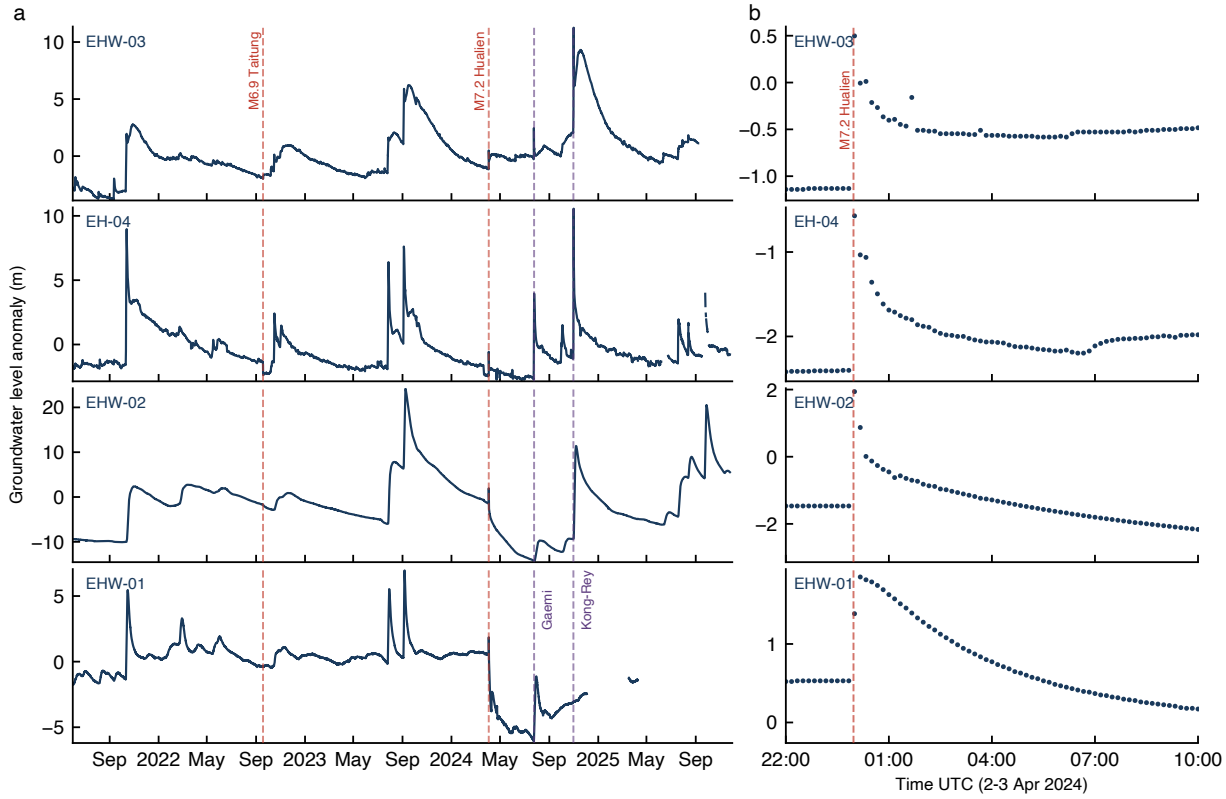


Figure 2: **Piezometric groundwater level records from Taroko National Park.** Panel **a** shows water level records for the study period from four wells. The water level exhibits step-like changes and alterations in drainage dynamics at the marked M6.9 Taitung and M7.2 Hualien earthquake sequences. Panel **b** shows a zoom-in on panel **a** of the hours following the 2024 M7.2 Hualien earthquake. For the tidal analysis, we use data from EHW-02.

wells, EHW-02 yields robust tidal-derived transmissivity estimates (see supplementary text) and, therefore, we centre the following analysis around results obtained from this well, which is located centrally within the Liwu catchment.

Until April 2024, the transmissivity deviates less than 20 % from its median value of $\sim 1.1 \times 10^{-6}$ m^2/s. Pump tests indicate a somewhat higher value of $\sim 1.7 \times 10^{-6}$ m^2/s (see Fig. 3) but validate the order of magnitude of the values retrieved from our tidal analysis. Regardless, as we analyse relative transmissivity changes, the accuracy of their absolute values is of lesser importance. Small variability in the transmissivity can often be explained by rising (falling) groundwater, which leads to lower (higher) effective stresses and thereby causes fracture apertures to increase (decrease) (*28*). To isolate co- and postseismic changes, we correct for this pore pressure effect (see Materials and Methods).

The pore pressure-corrected transmissivity exhibits several abrupt excursions. Two of these changes are transmissivity increases that coincided with large regional earthquakes — the 2022 M6.9 Taitung earthquake sequence and the 2024 M7.2 Hualien earthquake. Most prominently, following the Hualien earthquake, which caused ground-shaking of 0.5 g, the pore pressure-corrected transmissivity in EHW-02 increased by about 80 %. For about two weeks after the earthquake, our transmissivity estimate exhibits large uncertainties (see fig. S3), which may be due to high-frequency noise in the water level record. Therefore, we choose not to interpret the immediate transmissivity response to the M7.2 earthquake. Over the rest of the study period, the pore pressure-corrected transmissivity gradually decreased, albeit overprinted by two step decreases. A more subtle transmissivity increase of ~30 % occurred with the September 2022 Taitung earthquakes that induced a moderate peak ground acceleration (PGA) of <0.1 g. After those events, the transmissivity recovered over about 10 months to pre-earthquake levels.

Two further, distinct transmissivity decreases occurred well separated from any earthquakes within the time series. Specifically, four months after the Hualien earthquake, the transmissivity dropped by ~55 % of its pre-earthquake value coincident with the landfall of typhoon Gaemi. The raw transmissivity even dropped to values below its pre-earthquake baseline. Another ~25 % decrease coincided with typhoon Kong-Rey, three months later. Notably, we find no imprint on the transmissivity from typhoons before the 2024 Hualien earthquake, although some delivered more than twice Gaemi's rainfall (see Fig. 4). After the two typhoons in 2024, transmissivity values have

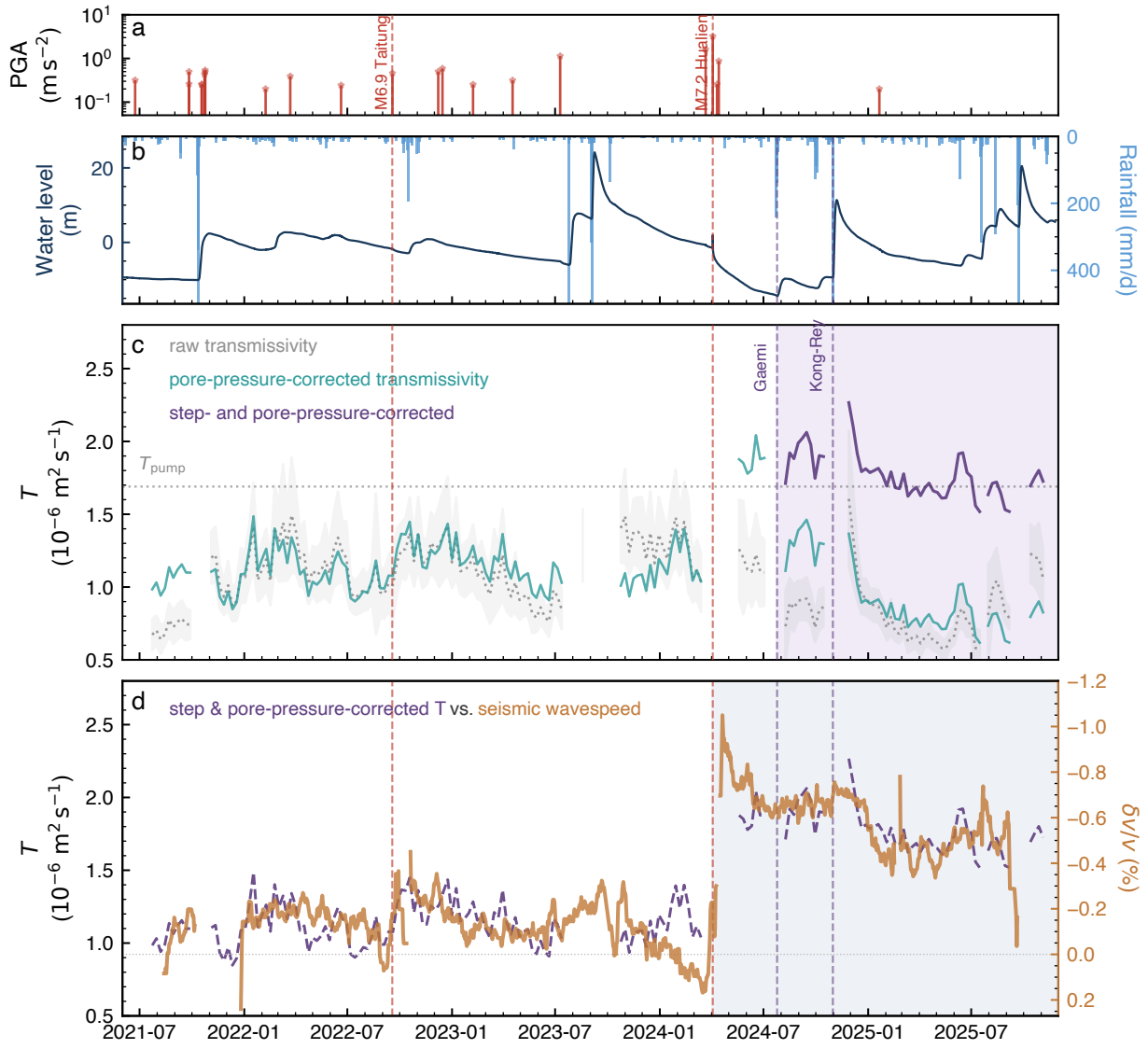


Figure 3: **Co-evolution of the transmissivity and the seismic wavespeed** ($\delta v/v$)**. a** Peak ground accelerations (PGAs) measured for regional earthquakes $M \geq 4.5$. **b** Piezometric water level records measured at EHW-02 and daily rainfall at the automatic weather station C0T820. **c** From tidal inversion, we retrieve the raw transmissivity (dotted grey curve) and its $\pm\sigma$ error envelopes. For comparison, we show the transmissivity estimated from hydraulic pump tests T_{pump}. We apply a pore pressure correction (teal curve) and remove steps introduced by the typhoons Gaemi and Kong-Rey (purple curve). **d** The low-frequency seismic wavespeed co-evolves with the fully corrected transmissivity. The shading in panel c emphasises the typhoon-induced, lasting transmissivity decrease, while panel d is shaded for times following the Hualien earthquake. We computed $\delta v/v$ from data in the frequency band 0.5-1 Hz from station TQ01. We exclude $\delta v/v$ values with a correlation coefficient of $R_{av} < 0.25$ and transmissivity values with standard deviations $> 5 \times 10^{-7}$ m^2/s. Note that the $\delta v/v$ axis is inverted.

not recovered to background values within the study period.

Seismic wavespeed changes

As a measure of the solid substrate's rock mechanical state, we consider seismic wavespeed changes ($\delta v/v$). To obtain $\delta v/v$ estimates for several depth ranges, we compute $\delta v/v$ from several frequency bands, where higher frequencies result in $\delta v/v$ estimates for shallower depths (*29*). High-frequency $\delta v/v$ is anticorrelated with water level, which is expected from the pressure-dependency of the elastic properties [e.g., (*30–32*)]. Here, we aim to analyse properties of the substrate independently from groundwater level variations in the aquifer. Therefore, we focus the analysis on low-frequency (0.5-1 Hz) $\delta v/v$ (representative example from station TQ01 in Fig. 3d) that shows only minimal impacts of water level fluctuations (see figs. S4 and S5).

Within these low-frequency $\delta v/v$ time series, we find two significant drops. Both of these drops occurred coseismically with the 2022 Taitung earthquakes and the 2024 Hualien earthquake and with amplitudes of 0.25 % and 0.8 %, respectively. The drops are followed by periods of postseismic recovery: the seismic wavespeed drop induced by the Taitung earthquakes recovered after about 10 months, while the postseismic recovery transient following the Hualien earthquake continued throughout the remainder of the time series.

Discussion

Earthquakes and typhoons induced two kinds of transmissivity changes

The two most striking features in the comparison of evolution of the seismic wavespeed and the pore pressure-corrected transmissivity are their co-evolution in the co- and postseismic periods of the 2022 and 2024 earthquakes and their divergence in response to the 2024 typhoons. Importantly, the only coseismic transmissivity changes in the four-year time window covered by this study coincide with the only coseismic wavespeed changes. Furthermore, coseismic transmissivity increases are not only accompanied by decreases in $\delta v/v$, but the ensuing postseismic recovery to a base value follows similar trajectories. This co-evolution holds across all stations and for depth ranges $>\sim 200$ m (see figs. S6 and S7). Shallower depths show residuals of groundwater signals — even after correction.

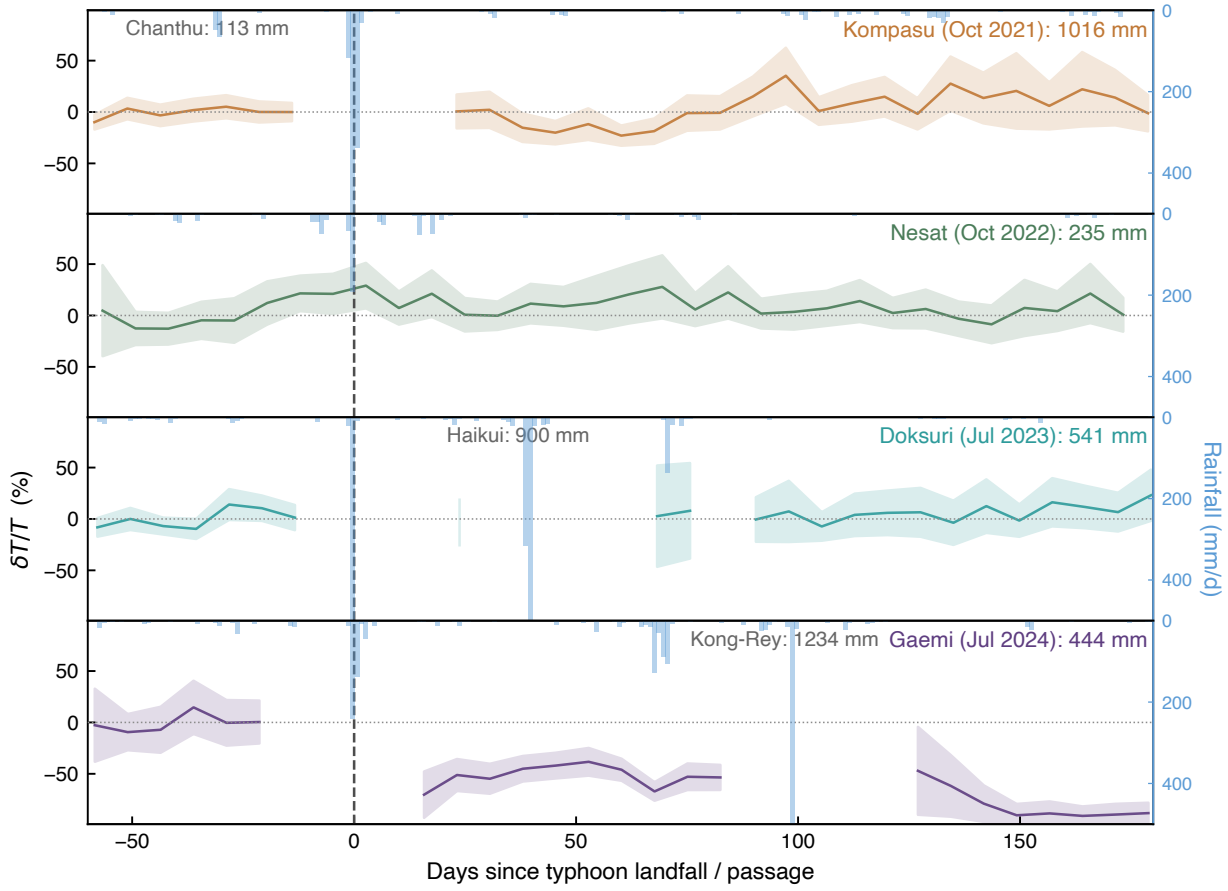


Figure 4: **Transmissivity response to major typhoons.** The relative pore pressure-corrected transmissivity ($\delta T/T$) only shows a statistically significant change in response to the Gaemi and Kong-Rey typhoons, which occur ~four and seven months after the 2024 M7.2 Hualien earthquake. For all other typhoons, including Nesat that follows the significantly smaller Taitung earthquakes, no change is detectable. For $\delta T/T$, we show the $\pm\sigma$ error envelopes. We exclude $\delta T/T$ values with $\sigma > 50\,\%$. For each typhoon, we indicate the total rainfall ± 3 days from its occurrence. Data gaps result from increased noise level in the tidal inversion due to barometric fluctuations and strong water level changes.

Unlike the local transmissivity, the seismic wavespeed does not show any changes unrelated to pore pressure changes following the 2024 Gaemi and Kong-Rey typhoons.

The sequence of an earthquake followed by two typhoons provides two independent diagnostics for the mechanisms behind each transmissivity change. As a first diagnostic, mechanisms that modify the substrate as a whole, such as pervasive changes in pore space geometry, should affect both the transmissivity and the seismic wavespeed. By contrast, mechanisms confined to the groundwater system, such as fracture clearing or clogging, should affect only the transmissivity. Second, the typhoons struck while the groundwater system was still recovering from the earthquake impact; had both types of perturbation acted through the same mechanism, then, the typhoons should have altered the postseismic recovery trajectories of the seismic wavespeed and the transmissivity. Both diagnostics separate the two kinds of change: the wavespeed responds only to the earthquakes, and the postseismic transmissivity recovery trend continues through the typhoon season. Below, we use these diagnostics to test candidate mechanisms. We start with the typhoon-induced decreases, because the mechanism we identify for them is needed to constrain the cause of the coseismic increases.

The 2024 typhoon season

There is a sharp contrast in the response of the groundwater system to typhoons before and after the 2024 Hualien earthquake: typhoons typically do not impact the transmissivity beyond direct water level effects, but, in the months after the earthquake, typhoons produced lasting and substantial transmissivity decreases (Fig. 4). We do not find a change in the groundwater system's response to rainfall following any other earthquake, including the 2022 Taitung sequence, raising the question how the Hualien event differed from preceding earthquakes. Compared to the larger Hualien earthquake, all other earthquakes produced substantially less coseismic landsliding (*33, 34*) and presumably also loosened less sediment that could have been mobilised during subsequent typhoons (*35, 36*). Such sediment can drive local transmissivity changes in two ways: increased effective stress from sediments redeposited by typhoon-induced flooding, or fracture clogging by sediment particles (*16*). Two observations are inconsistent with increased effective stress by redeposited sediment as the driving mechanism. First, we estimate that the added sediment thickness needed to produce the first typhoon-induced transmissivity drop alone is at least $\sim$ 5 m (see

Materials and Methods). Such deposition may have occurred at select locations, but overall, in mountain landscapes, typhoons cause erosion rather than deposition (*37*), reducing effective stress at landscape scale. Second, effective stress modifications impact the seismic wavespeed. However, for the 2024 typhoons, we do not observe wavespeed changes unrelated to pore pressure changes. We can thus rule out effective stress modifications as the mechanism for the 2024 typhoon-induced transmissivity changes.

Fracture clogging by sediment (*16*), capable of decreasing transmissivity, may have been enabled by the combination of surface fracturing due to strong ground motion, increased sediment availability through coseismic mass wasting, and typhoon-induced overland flow and infiltration capable of injecting sediments deeper into the fracture network. Because the effect of clogging on the elastic properties of the bulk substrate is likely negligible, it does not noticeably impact the seismic wavespeed. Our transmissivity observations suggest that typhoons do not only deliver sediments to rivers (*38*) but also flush them into groundwater systems. In our study area, typhoon rainfall generates overland flow, as previously inferred from the chemical and isotopic composition of Liwu River water during typhoons (*25*). Rapid flooding of open fissures by this flow creates large pressure gradients that can drive pervasive sediment injection within hours to days (*39, 40*). Large earthquakes prime this mechanism in two complementary ways: they generate sediment across steep mountain terrain (*36, 41*), and they open and widen macrofractures that increase the infiltration capacity of the landscape and allow sediment particles to reach deeper parts of the groundwater system (*42, 43*). Smaller earthquakes before the Hualien earthquake likely were insufficient to change crack opening at the surface pervasively and generated insufficient sediment in our study area to facilitate fracture clogging. This delayed earthquake-primed but typhoon-triggered fracture clogging has not been previously identified.

Co- and postseismic transmissivity changes

Unlike the typhoon-induced drops, the coseismic transmissivity increases that we observe for the 2022 Taitung and 2024 Hualien earthquakes were accompanied by wavespeed decreases and they recovered over time. Such transmissivity increases could be linked to coseismic static stress changes (*12*), unclogging or clearing of fractures by seismic wave passage (*11, 16, 44*), or changes in fracture geometry that enhance connectivity (*28*), but no single mechanism has been universally

agreed on.

Coseismic static stress changes have generally been discarded as a major cause of seismic wavespeed changes, as they cannot explain the spatial pervasiveness, the sign consistency (almost invariably negative), or the logarithmic recovery of wavespeed changes (*19, 20*). Moreover, the Taitung earthquake would not have caused significant static stress changes at our site due to its relatively large epicentral distance.

Clearing of fractures by seismic shaking, opposite to the mechanism we invoked for the typhoon-induced transmissivity drop, could cause transmissivity to increase (*44*), but we dismiss this mechanism as the main driver of the coseismic transmissivity increase for two reasons. First, if clearing of fractures was the dominant driver of the coseismic transmissivity increase, its gradual postseismic recovery would correspond to progressive refilling of fractures. Within this hypothetical framework, typhoon-induced sediment injection would accelerate such refilling and disrupt or even reset the postseismic recovery trajectory. Instead, we observe an unbroken postseismic transmissivity recovery, which indicates that coseismic and typhoon-triggered transmissivity changes stem from two unrelated processes that do not directly interact on a microscopic level. Second, as clearing or clogging of pore spaces does not impact the seismic wavespeed, the parallel postseismic recovery of the seismic wavespeed and the transmissivity would have to be coincidental.

Instead, we consider that seismically induced changes of rock fracture geometry likely simultaneously affected the seismic wavespeed and the permeability. The seismic wavespeed is controlled by the contact area within micro- and macrofractures (*45*). The permeability, on the other hand, depends mostly on the aperture of these fractures (*46*). Some processes, such as clearing and clogging of fractures, alter the effective hydraulic aperture (*46*) but do not affect the contact area. However, in some cases, for example, when changes in effective stress open or close fractures, these properties may covary. Because permeability scales with the cube of fracture aperture (*46*) while seismic wavespeed changes are proportional to grain contact area (*45*), a geometric change that widens fractures while reducing contact area produces permeability changes that far exceed wavespeed changes — consistent with our observation that relative transmissivity changes were two orders of magnitude larger than concomitant relative wavespeed changes (Fig. 3). Following the coseismic change, contact area and aperture of the fracture network recover on the same trajectory. Seismic wavespeed decreases and their recovery are an expression of the so-called nonclassical nonlinear

response of materials to stress changes, in which grain contacts are disrupted and recover logarithmically (*47–49*). The co-evolution of transmissivity and seismic wavespeed, and their parallel postseismic recovery, indicate that coseismic changes in fracture aperture and grain contact area are coupled, and that both recover on the timescale predicted by nonclassical nonlinear elasticity. The recovery of earthquake-induced fracture geometry changes was incomplete when typhoons Gaemi and Kong-Rey made landfall. This likely later allowed typhoon-mobilised sediment to percolate deeply into the groundwater network, where clogging narrowed the fractures without interrupting the geometric recovery of their contacts. This interpretation remains a hypothesis, but it is the only single-mechanism explanation consistent with all our observations.

The seismic wavespeed as a diagnostic tool for permeability changes

Earthquakes with similar intensity do not necessarily affect the groundwater system equally. In contrast to findings by (*11*), peak ground acceleration (PGA) is not a reliable measure for the amplitude or even the occurrence of a transmissivity change. In our time series, we find earthquakes producing higher PGAs than the 2022 Taitung earthquake that are not associated with discernible transmissivity changes (see Fig. 3), consistent with observations by (*22, 23*). For our data, we find that coseismic changes in seismic wavespeed are a good indicator for coseismic transmissivity modifications: every coseismic transmissivity change is accompanied by a coseismic variation in wavespeed and vice versa (see Fig. 3). This likely reflects differences in spatial sensitivities: the PGA is a point measure that is heavily influenced by local topography, near-surface geology, and source directionality (*50–52*), whereas the seismic wavespeed integrates changes over larger volumes (*29*). When the underlying transmissivity change is rock-mechanical, the seismic wavespeed may serve as a proxy for postseismic permeability recovery. However, when clogging or clearing dominates, as for the 2024 typhoons, the seismic wavespeed does not respond. Where continuous groundwater observations are available, the seismic wavespeed can become a discriminator of the underlying causes of transmissivity change.

Implications for postseismic water availability

Because the postseismic transmissivity transient follows a similar trajectory to that of the seismic wavespeed, we can use observations of seismic wavespeed recovery to infer expected recovery times of rock-mechanical transmissivity changes in the absence of sealing effects. Postseismic wavespeed recovery has been observed to take several months to over a decade [e.g., (*18, 20, 53–55*)]. This implies that groundwater volumes and flow rates will take similarly long to return to pre-earthquake baselines [as independently estimated by (*11, 56*)].

While previous studies have invoked fracture clogging as a coseismic mechanism (*10, 16, 21*), we demonstrate that it can manifest postseismically as an abrupt and substantial transmissivity drop, months after the earthquake, when sediments made available by coseismic ground shaking are flushed into the fracture network opened up by earthquake damage. For the following year, until the end of our time series, there is no sign of recovery from these transmissivity decreases in our data, indicating that the pervasive clogging of the millimetric-to-centimetric fractures that control permeability (*57*) may persist for years. This can cause significant discharge deficits in seismically perturbed catchments. In the case of the Liwu catchment, the observed typhoon-induced transmissivity decrease of about 50 % relative to pre-earthquake values caused discharge deficits estimated at 8–24 % (see Materials and Methods). Long-lasting groundwater perturbations are consistent with observed impacts on vegetation health in the years following large earthquakes (*58–60*). When, whether, and how clogged fractures are cleared, and transmissivity is restored to pre-earthquake values, remain important open questions, although earthquake-induced shaking (*11, 16*) or flushing by steep pressure gradients during intense rainfall on a landscape without open surface fissures could potentially drive fracture evacuation.

In steep landscapes like the Taiwan Central Range, transmissivity changes are unlikely to be spatially uniform. Topographic amplification focuses earthquake damage on mountain ridges (*50–52*), inducing stronger transmissivity changes and enhancing the known effect of postseismic redistribution of water from higher to lower elevations (*61*). Storm-driven clogging, on the other hand, will preferentially take place in valleys, where topography concentrates overland flow and sediment-laden flooding (*38*), further amplifying the difference between valley and ridge transmissivities. Such effects are most consequential at convergent plate boundaries, where steep landscapes and

megathrust earthquakes combine, altering permeability distributions within the mountain catchments that provide essential water services for years. Knowing the dynamic nature of the mountain groundwater systems and their response to sequenced seismic and meteorological perturbations will help to anticipate trends and changes in resource availability.

Materials and Methods

Groundwater records

We obtain water level records from four wells: EH-04, EHW-03, EHW-01, and EHW-02. Based on the lithological information, transfer function characteristics, pump test results and the drainage and recharge behaviour, we classify EHW-03 and EH-04 as unconfined wells. Their barometric transfer functions exhibit near-zero barometric efficiency, and tidal transfer functions derived from their piezometric records have broad optima leading to large uncertainties (i.e., $> 20°$ for the tidal phase), precluding reliable tidal inversion. EHW-01 samples a confined but very low-permeability formation ($T \approx 1\times10^{-8}$ m^2/s), for which semidiurnal tidal forcing is insufficient to drive measurable flow from the aquifer into the borehole within a half-tidal period. For these three wells, we only use their piezometric records to correct $\delta v/v$ for water-level-induced fluctuations (see "Water level compensation"). EHW-02, which samples a semi-confined fractured aquifer, delivers robust tidal transfer functions.

Geologically, eastern Taiwan is dominated by intense tectonic deformation resulting in an extraordinarily steep topography and a lithology dominated by metamorphic rocks. In particular, schists, marbles, and quartzites are prevalent. EHW-02 was drilled through a sequence of fractured schists overlain by ~17 m of colluvium. The resulting borehole was cased and closed to isolate it from atmospheric influences. The well is screened between 85 and 97 m depth at a 10 min sampling interval and logged as groundwater level above sea level in metres. To obtain the groundwater level anomaly time series shown in the manuscript, we demean the data.

Computing transmissivity time series from well records, solid Earth tides, and barometric records

To obtain the transmissivity time series, we closely follow the procedure proposed by (*23*), who extended earlier work by (*17*) and (*62*) to compute such time series from tidal areal strain time series, barometric records, and groundwater level records for semi-confined aquifers. The algorithm consists of a two-step procedure: First, the tidal and barometric transfer functions of the groundwater level are computed for narrow frequency bands. Thereafter, one can invert for the aquifer's transmissivities $T(t)$ and shear moduli $G(t)$ that minimise the misfit to the observed transfer functions. This inversion requires knowledge of some well specifications and hydraulic parameters that can be derived from pump tests. Aside from assuming a constant vertical diffusivity D' for the leaky aquitard, we follow the procedure described in (*23*).

Like previous authors, we focus our analysis on tidal modes around the semi-diurnal tidal bands, including the M2, N2, and S2 modes, which separate more cleanly from harmonic noise than diurnal tides (*11, 17, 23, 62*). To avoid introducing high-frequency noise into our analysis, we detrend and taper the data before applying a simple spike and step removal that removes water level changes above 2.5 cm per 10 min. Then, we bandpass filter the piezometric time series between 1.6 and 2.4 cycles per day using a 4th-order zero-phase Butterworth filter, effectively removing harmonic noise outside our band of analysis. To decrease the computational cost of the remaining steps, we decimate the water level and tidal data to a 60 min sampling interval.

To obtain the tidal and barometric transfer functions (i.e., time-dependent functions for barometric and tidal gain and phase lag), we apply a harmonic least-squares fit to the areal solid Earth tide strain, the barometric pressure, and the bandpass-filtered water level; thereby, we obtain complex functions containing amplitude and phase for each of the three frequencies. As in (*22*), we assume each frequency component k of the piezometric record to be the linear sum of the barometric and the tidal forcing:

$$\forall k \in [1, n], \tilde{h}_k = \frac{1}{\rho g}(Z_{a,k}\tilde{P}_k + Z_{\epsilon,k}\tilde{\epsilon}_k) \tag{1}$$

where $\tilde{h}$, $\tilde{P}$, and $\tilde{\epsilon}$ are the complex amplitudes of the piezometric water level, the atmospheric pressure, and the tidal strain, respectively. We set $\rho = 1000\,\frac{\mathrm{kg}}{\mathrm{m}^3}$ and $g = 9.81\,\frac{\mathrm{m}}{\mathrm{s}^2}$. To solve for the barometric and tidal transfer functions Z_a and Z_ϵ, we need to extract the values for at least

two frequencies. It further requires us to assume that the frequency dependency between those frequencies is negligible (*63*). Here, we solve for three quasi-semidiurnal frequencies (M2, N2, and S2), allowing us to create an overconstrained system of linear equations, to which we apply a complex least-squares solve, thereby obtaining additional uncertainty estimates:

$$\begin{aligned} \rho g \tilde{h_1} &= Z_a \tilde{P}_1 + Z_\epsilon \tilde{\epsilon}_1 \\ \rho g \tilde{h_2} &= Z_a \tilde{P}_2 + Z_\epsilon \tilde{\epsilon}_2 \\ \rho g \tilde{h_3} &= Z_a \tilde{P}_3 + Z_\epsilon \tilde{\epsilon}_3 \end{aligned} \tag{2}$$

We solve this equation for time steps of 29.5 days (i.e., one lunar month) and in increments of 7.5 days. To refine our uncertainty estimates, we bootstrap the result 2000 times. We show the resulting transfer functions $Z_a(t)$ and $Z_\epsilon(t)$ in fig. S2.

Finally, to obtain $T(t)$ from the estimated transfer functions, we use the solution for a two-layered model by (*23*) that requires us to solve two partial differential equations for the atmospheric pressure and the tidal response:

$$T\nabla^2 h + q = S(\frac{\partial h}{\partial t} - \frac{\gamma}{\rho g}\frac{\partial P}{\partial t}) \tag{3}$$

$$T\nabla^2 h + q = S(\frac{\partial h}{\partial t} - \frac{2\gamma G}{\rho g}\frac{\partial \epsilon}{\partial t}) \tag{4}$$

where q is the vertical leakage flow, G the aquifer's shear modulus, γ its uniaxial Skempton coefficient or loading efficiency, T the transmissivity, and S the storativity. The full solution is provided in (*23*). In contrast to them, we solve the equation for a time-invariant vertical diffusivity $\frac{\mathrm{d}D'}{\mathrm{d}t} = 0$, which reduces the number of unknowns and thereby decreases the noise level in the inversion procedure. We characterise the upper layer as a leaky aquitard with a thickness of 20 m and a storativity of $S' = 8 \times 10^{-4}$, and the lower layer as an aquifer with a storativity of $S = 7.2 \times 10^{-5}$ (see "Aquifer and aquitard properties inferred from pump tests"). Furthermore, the algorithm requires us to define the well's screen and casing radii, which are $r_w = r_c = 0.0254$ m.

As we do not have any direct measurements of the uniaxial Skempton coefficients γ and γ' and the hydraulic diffusivity D', we calibrate them directly from the transfer functions. To this end, we exploit the dependency of the loading efficiency ratio $R = \frac{1-\gamma'}{1-\gamma}$, required to calibrate our model, on the median phase difference between tidal and barometric transfer functions $\tilde{\Delta\phi} \approx 19°$ and the vertical diffusivity D' (as described in appendix B2 of (*23*)). For a given D', we find the

R that produces this phase difference analytically. We independently assess numerical stability by checking the fraction of time steps at which the inversion pins at its search bounds across a range of D'-R pairs, preferring pairs that minimise this fraction. This procedure yields $R \approx 0.23$ and $D' \approx 2.1 \times 10^{-3} \frac{m^2}{s}$, agreeing to first order with independent pump test results (see "Aquifer and aquitard properties inferred from pump tests"). Finally, we invert for $T(t)$ from the tidal phase response. The tidal amplitude gain and $T(t)$ constrain the shear modulus $G(t)$, which we do not interpret for reasons laid out in "Postprocessing the transmissivity".

Postprocessing the transmissivity

Removing the water level dependency in $T(t)$ We find a subtle water level dependency for $T(t)$. Higher pore pressures lead to an extension of existing pores and cracks, increasing their permeability. This dependency can be corrected as demonstrated by (*23*). We do so by fitting our observations of transmissivity and effective stress changes to a model relating the two (*28*):

$$\left(\frac{T}{T_0}\right)^{1/3} = 1 - \alpha \ln \frac{\sigma^*}{\sigma_0^*} \tag{5}$$

where σ^* is the effective stress, T_0 and σ_0^* are the mean transmissivity and mean effective stress, respectively. α is the proportionality coefficient that we find through a least-squares misfit optimisation in a simple gridsearch process. To avoid noise introduced by co- and postseismic transmissivity changes, we only consider observations before the Hualien earthquake. The resulting correction and fit are shown in fig. S3.

Step removal in $T(t)$ Coinciding with the Gaemi typhoon, we find a step decrease in T (see Results) of $-6 \times 10^{-7}\mathrm{m}^2/\mathrm{s}$. For Kong-Rey, the corresponding step is $-3 \times 10^{-7}\mathrm{m}^2/\mathrm{s}$. To facilitate the comparison of the postseismic transient behaviours in $\delta v/v$ and T, we remove these steps simply by subtracting them from the time series following each typhoon's landfall.

Water level dependency in $G(t)$ We find a strong positive correlation between the tidal transfer function's gain and the piezometric water level, which carries through into the inferred $G(t)$ (see figs. S2 and S3). As structural shear modulus changes and pore pressure-induced gain changes are in practice indistinguishable, we chose not to interpret $G(t)$. $T(t)$ is unaffected as it is derived solely from the tidal phase response.

Estimating sediment load changes

After finding α for Eq. 5, we can simply infer the amount of effective stress required to produce the observed typhoon-triggered transmissivity changes from the fitted model. As a lower-bound estimate, we assume drained conditions, i.e. we set the Skempton coefficient to 0. The thickness of newly deposited sediment required to produce the step change introduced only by typhoon Gaemi ($-6 \times 10^{-7}\,\mathrm{m}^2/\mathrm{s}$) is 4.8 m, assuming a mass density of $1800\,\mathrm{kg/m}^3$.

Aquifer and aquitard properties inferred from pump tests

The Geological Survey and Mining Management Agency performed hydraulic pump tests at our borehole site (see table S1). These tests yielded values for the specific storativity S_s and the hydraulic conductivity K at various depth ranges. We infer storativity values for aquifer and aquitard and transmissivity values for the aquifer from these values. Specifically, we obtain $T_{PT}^{87-100\,\mathrm{m}} = K\Delta h = 1.3 \times 10^{-7}\,\mathrm{m/s} \times 13\,\mathrm{m} = 1.69 \times 10^{-6}\,\mathrm{m}^2/\mathrm{s}$ assuming an isotropic hydraulic conductivity. We plot this value as reference in Fig. 3. We directly take $S = 7.2 \times 10^{-5}$ from the depth range of 28 to 100 m. For the aquitard, we choose the geometric mean, $S' = 8 \times 10^{-4}$, computed from the S values derived from the intervals 30-31.5 m with $S_s = 1.1 \times 10^{-5}\,\mathrm{m}^{-1}$ and 39-40.5 m depth with $S_s = 1.4 \times 10^{-4}\mathrm{m}^{-1}$, yielding $S' = S'_s \times h' = 2.2 \times 10^{-4}$ and $S' = 2.8 \times 10^{-3}$, respectively, assuming an aquitard thickness of $h' = 20\,\mathrm{m}$. We can also use these values to validate our choice for D' as $D' = K'/S'_s$ (*64*), again assuming an isotropic hydraulic conductivity. Using this relation, we obtain values spanning between $7.86 \times 10^{-5}\,\mathrm{m}^2/\mathrm{s}$ and $2.45 \times 10^{-3}\,\mathrm{m}^2/\mathrm{s}$, depending on the chosen depth range - placing our chosen $D' \approx 2.1 \times 10^{-3}\,\mathrm{m}^2/\mathrm{s}$ at the upper end of the range. Generally, pump test values vary by around one order of magnitude, depending on the depths from which they were derived, leaving substantial room for data uncertainty.

Obtaining seismic wavespeed changes from ambient seismic noise

To obtain the $\delta v/v$ time series, we follow the stretching method as proposed by (*24*) and implemented in the SeisMIC software package (*65*). During preprocessing, we taper, detrend, anti-alias filter, and decimate the data to 5, 10, 12.5, 25, or 50 Hz, depending on the octave frequency band in which we subsequently bandpass filter. Our chosen frequency bands, 0.5-1 Hz, 1-2 Hz, 2-4 Hz, 4-8 Hz,

and 8-16 Hz, provide us with depth sensitivities of tens of metres (16 Hz) down to 1-2 km (0.5 Hz) (*29*). Finally, we impose one-bit-normalisation and whiten their amplitude spectra (*66*).

The actual algorithm to retrieve relative seismic wavespeed changes consists of a two-step procedure: First, one correlates continuous seismic data from time t_n to remove the source-side effect, extracting empirical Green's functions (EGFs). Thereafter, the EGF from t_n is stretched against a reference to obtain a homogeneous velocity change at t_n (see (*65*) for a detailed description of the algorithm). In practice, we cross-correlate hourly seismic data recorded on the three directional components (vertical, north, east), thereby obtaining three cross-component correlations or EGFs per station (E-N, E-Z, and N-Z). To estimate $\delta v/v(t)$, we compare 2-week-long averages of those EGFs with stretched versions of the temporal average of all EGFs, which acts as our reference, corresponding to 0 % velocity change. Specifically, we compare the early coda of the EGFs between lag times of $\tau_s = 5/T_0$ and $\tau_e = 10/T_0$, where T_0 is the low-corner period of the applied bandpass filter. This early coda is dominated by surface waves, for which our depth estimates are valid (*29*). We find the wavespeed change for each day by stretching the reference by up to 5 % and identifying the stretching factor producing the highest correlation for each daily smoothed EGF. We then apply a weighted average to the three $\delta v/v$ estimates from each station (*67*), obtaining one $\delta v/v$ curve per station with a one-day sampling interval. For representation purposes, we roll the results so that the 1st February 2024 has 0 % wavespeed change.

Quality controlling $\delta v/v$

In eastern Taiwan, extreme weather events lead to flooding, sliding, and slumping that affect the sensors. As a result, stations may fail, or their ground coupling may deteriorate. Generally, we disregard stations without available data around the M7.2 Hualien earthquake or whose data quality does not satisfy the threshold described below. As a result, we discard six stations from our analysis: TQ00, TQ03, TQ04, TQ05, TQ07, and TQ11 (none of which is plotted in Fig. 1).

The quality of a $\delta v/v$ estimate can be assessed using the correlation coefficient between the stretched reference and the daily correlation function. After averaging the three components, we obtain an average correlation coefficient that is inherently lower than the individual values but still represents a reliable measure for the stability of each $\delta v/v(t_n)$ (*67*). After inspection, we opt to discard $\delta v/v$ time series that exhibit significant portions of data points with $R_{av} < 0.4$. As a result,

we consider only some frequency bands for some stations.

Water level compensation

To remove the influence of groundwater fluctuations on $\delta v/v$, we compute linear fitting coefficients for a simple least-squares fit between each $\delta v/v$ and the water level curve with a soft L1 loss criterion, where the loss function is defined as $\rho(z) = 2(\sqrt{1+z} - 1)$ and z corresponds to the least-squares loss (*68*). We estimate the linear fitting coefficients for all $\delta v/v$ points with $R_{av} > 0.25$ and the period before the Hualien earthquake to avoid the influence of the coseismic wavespeed drop and postseismic recovery. Finally, the water-level-corrected version of $\delta v/v$ is then:

$$(\delta v/v)_{corr}(t) = (\delta v/v)(t) - (\delta v/v)_{lqm}(t) \tag{6}$$

where $(\delta v/v)_{lqm}$ is the modelled pore pressure-induced seismic wavespeed change.

Peak ground acceleration

To compute the PGA, we download data from stations F072 and F026 from the Taiwan Strong Motion Instrumentation Program Network (TSMIP), a network of force-balance accelerometers. Data are downloaded for the five minutes following the origin time of each seismic event with $M \geq 4.5$, hypocentral depth $z \leq 40\,\text{km}$, longitude $120° \leq \lambda \leq 121.5°$, and a latitude of $22.5° \leq \phi \leq 25.5°$. From the resulting traces, we remove the instrumental response and determine the envelope's maximum for each of the instrument's three components. We define the maximum value for each event as the event's PGA. For events after 07 April 2022, we consider the PGA from F072, which is co-located with well EHW-02 but has no available data before this date. We do not plot PGAs below a threshold of $0.2\,\text{m/s}^2$.

Translating transmissivity perturbations to discharge deficits

To estimate the potential catchment-scale consequence of the typhoon-induced transmissivity decrease, we use a deliberately simple first-order calculation. Its purpose is not to reproduce the transient groundwater response of the Liwu catchment but to bracket how a spatially distributed transmissivity reduction could affect cumulative discharge at the catchment outlet.

We consider the period from typhoon Kong-Rey (31 October 2024) to the latest available precipitation record (31 May 2026; $\Delta t \approx 1.58$ yr). Over this period, station C0T820 recorded a cumulative precipitation of $P = 4183.5$ mm. We approximate actual evapotranspiration as 700 mm/yr, i.e., $ET \approx 1106$ mm. Neglecting changes in long-term storage and deep groundwater losses, the reference volume available for discharge from the catchment area $A = 616.3\,\mathrm{km}^2$ is

$$V_0 = (P - ET)\,A \approx 1.90\,\mathrm{km}^3 \tag{7}$$

which corresponds to a mean discharge of $Q_0 = V_0/\Delta t \approx 38\,\mathrm{m}^3/\mathrm{s}$.

We assume that a fraction f of the catchment experiences a fractional transmissivity decrease r, and that outlet discharge scales linearly with the spatially averaged transmissivity. The relative discharge deficit and the cumulative volume deficit are then

$$\frac{\Delta Q}{Q_0} = fr, \qquad \Delta V_Q = V_0\, fr \tag{8}$$

independent of the absolute background transmissivity. For $f = 20$–40 % and $r = 40$–60 % (bracketing the ∼50 % decrease observed at EHW-02), we obtain relative deficits of 8–24 %, or $\Delta V_Q \approx 0.15$–$0.46\,\mathrm{km}^3$. The calculated volume should not be interpreted as water that physically disappears from the catchment. It is more appropriately described as a potential cumulative outlet-flow deficit relative to a hypothetical catchment in which the transmissivity perturbation had not occurred. In other words, the calculated volume represents water that, according to the simple transmissivity scaling adopted here, would have reached the outlet during the considered period in the absence of fracture clogging but may not yet have done so in the perturbed system.

References and Notes

1. T. Gleeson, K. M. Befus, S. Jasechko, E. Luijendijk, M. B. Cardenas, The Global Volume and Distribution of Modern Groundwater. *Nature Geoscience* **9** (2), 161–167 (2016), doi: 10.1038/ngeo2590.

2. Richard Connor, Michela Miletto, *The United Nations World Water Development Report 2022: Groundwater: Making the Invisible Visible; Executive Summary*, Tech. Rep. 0000380726, UNESCO World Water Assessment Programme, France (2022).

3. S. S. D. Foster, P. J. Chilton, Groundwater: The Processes and Global Significance of Aquifer Degradation. *Philosophical Transactions of the Royal Society B: Biological Sciences* **358** (1440), 1957–1972 (2003), doi:10.1098/rstb.2003.1380.

4. L. Pelascini, P. Steer, M. Mouyen, L. Longuevergne, Modelling the Control of Groundwater on Landslides Triggering: The Respective Role of Atmosphere and Rainfall during Typhoons. *Natural Hazards and Earth System Science* (2022), doi:10.5194/nhess-2021-340.

5. Z. Shi, G. Wang, M. Manga, C.-Y. Wang, Continental-Scale Water-Level Response to a Large Earthquake. *Geofluids* **15** (1-2), 310–320 (2015), doi:10.1111/gfl.12099.

6. C. H. Mohr, M. Manga, C.-Y. Wang, O. Korup, Regional Changes in Streamflow after a Megathrust Earthquake. *Earth and Planetary Science Letters* **458**, 418–428 (2017), doi:10. 1016/j.epsl.2016.11.013.

7. C.-Y. Wang, M. Manga, New Streams and Springs after the 2014 Mw6.0 South Napa Earthquake. *Nature Communications* **6** (1), 7597 (2015), doi:10.1038/ncomms8597.

8. Z. Jin, *et al.*, Seismically Enhanced Solute Fluxes in the Yangtze River Headwaters Following the A.D. 2008 Wenchuan Earthquake. *Geology* **44** (1), 47–50 (2016), doi:10.1130/G37246.1.

9. Z. Biais, C. Andermann, P. Steer, L. Longuevergne, Substantial Excess Groundwater Release Following the 2015 Gorkha Earthquake in Nepal. *ESS Open Archive* **2026** (0609), doi:10. 22541/essoar.15004547/v1.

10. M. Manga, *et al.*, Changes in Permeability Caused by Transient Stresses: Field Observations, Experiments, and Mechanisms. *Reviews of Geophysics* **50** (2) (2012), doi:10.1029/2011RG000382.

11. J. E. Elkhoury, E. E. Brodsky, D. C. Agnew, Seismic Waves Increase Permeability. *Nature* **441** (7097), 1135–1138 (2006), doi:10.1038/nature04798.

12. R. Muir-Wood, G. C. P. King, Hydrological Signatures of Earthquake Strain. *Journal of Geophysical Research: Solid Earth* **98** (B12), 22035–22068 (1993), doi:10.1029/93JB02219.

13. C. H. Mohr, M. Manga, C.-y. Wang, J. W. Kirchner, A. Bronstert, Shaking Water out of Soil. *Geology* **43** (3), 207–210 (2015), doi:10.1130/G36261.1.

14. Z. Shi, G. Wang, Aquifers Switched from Confined to Semiconfined by Earthquakes. *Geophysical Research Letters* **43** (21), 11,166–11,172 (2016), doi:10.1002/2016GL070937.

15. C.-Y. Wang, X. Liao, L.-P. Wang, C.-H. Wang, M. Manga, Large Earthquakes Create Vertical Permeability by Breaching Aquitards. *Water Resources Research* **52** (8), 5923–5937 (2016), doi:10.1002/2016WR018893.

16. E. E. Brodsky, E. Roeloffs, D. Woodcock, I. Gall, M. Manga, A Mechanism for Sustained Groundwater Pressure Changes Induced by Distant Earthquakes. *Journal of Geophysical Research: Solid Earth* **108** (B8) (2003), doi:10.1029/2002JB002321.

17. P. A. Hsieh, J. D. Bredehoeft, J. M. Farr, Determination of Aquifer Transmissivity from Earth Tide Analysis. *Water Resources Research* **23** (10), 1824–1832 (1987), doi:10.1029/WR023i010p01824.

18. F. Brenguier, *et al.*, Postseismic Relaxation Along the San Andreas Fault at Parkfield from Continuous Seismological Observations. *Science* **321** (5895), 1478–1481 (2008), doi:10.1126/science.1160943.

19. M. Gassenmeier, *et al.*, Field Observations of Seismic Velocity Changes Caused by Shaking-Induced Damage and Healing Due to Mesoscopic Nonlinearity. *Geophysical Journal International* **204** (3), 1490–1502 (2016), doi:10.1093/gji/ggv529.

20. L. Illien, J. M. Turowski, C. Sens-Schönfelder, C. Berenfeld, N. Hovius, Predictable Recovery Rates in Near-Surface Materials after Earthquake Damage. *Nature Communications* **16** (1), 1790 (2025), doi:10.1038/s41467-025-57151-8.

21. B. Vittecoq, J. Fortin, J. Maury, S. Violette, Earthquakes and Extreme Rainfall Induce Long Term Permeability Enhancement of Volcanic Island Hydrogeological Systems. *Scientific Reports* **10** (1), 20231 (2020), doi:10.1038/s41598-020-76954-x.

22. A. Thomas, J. Fortin, B. Vittecoq, S. Violette, Earthquakes and Heavy Rainfall Influence on Aquifer Properties: A New Coupled Earth and Barometric Tidal Response Model in a Confined Bi-Layer Aquifer. *Water Resources Research* **59** (4), e2022WR033367 (2023), doi: 10.1029/2022WR033367.

23. A. Thomas, *et al.*, Hydro-Mechanical Characterization of a Fractured Aquifer Using Groundwater Level Tidal Analysis: Effect of Pore Pressure and Seismic Dynamic Shear Stresses on Permeability Variations. *Journal of Geophysical Research: Solid Earth* **129** (8), e2024JB028847 (2024), doi:10.1029/2024JB028847.

24. C. Sens-Schönfelder, U. Wegler, Passive Image Interferemetry and Seasonal Variations of Seismic Velocities at Merapi Volcano, Indonesia. *Geophysical Research Letters* **33** (21), 1–5 (2006), doi:10.1029/2006GL027797.

25. D. Calmels, *et al.*, Contribution of Deep Groundwater to the Weathering Budget in a Rapidly Eroding Mountain Belt, Taiwan. *Earth and Planetary Science Letters* **303** (1), 48–58 (2011), doi:10.1016/j.epsl.2010.12.032.

26. J.-M. Chang, W.-A. Chao, C.-M. Yang, M.-W. Huang, Coseismic and Subsequent Landslides of the 2024 Hualien Earthquake (M7.2) on April 3 in Taiwan. *Landslides* **21** (10), 2591–2595 (2024), doi:10.1007/s10346-024-02312-x.

27. X. Huang, J. C. L. Chan, L. Bai, Z. Yu, T. Sun, Tropical Cyclone Activities in the Western North Pacific in 2024. *Tropical Cyclone Research and Review* **15** (1), 29–42 (2026), doi: 10.1016/j.tcrr.2026.01.004.

28. J. B. Walsh, Effect of Pore Pressure and Confining Pressure on Fracture Permeability. *International Journal of Rock Mechanics and Mining Sciences & Geomechanics Abstracts* **18** (5), 429–435 (1981), doi:10.1016/0148-9062(81)90006-1.

29. A. Obermann, T. Planès, E. Larose, C. Sens-Schönfelder, M. Campillo, Depth Sensitivity of Seismic Coda Waves to Velocity Perturbations in an Elastic Heterogeneous Medium. *Geophysical Journal International* **194** (1), 372–382 (2013), doi:10.1093/gji/ggt043.

30. T. Clements, M. A. Denolle, Tracking Groundwater Levels Using the Ambient Seismic Field. *Geophysical Research Letters* **45** (13), 6459–6465 (2018), doi:10.1029/2018GL077706.

31. T. Lecocq, L. Longuevergne, H. A. Pedersen, F. Brenguier, K. Stammler, Monitoring Ground Water Storage at Mesoscale Using Seismic Noise: 30 Years of Continuous Observation and Thermo-Elastic and Hydrological Modeling. *Scientific Reports* **7** (1) (2017), doi:10.1038/s41598-017-14468-9.

32. S. Mao, A. Lecointre, R. D. van der Hilst, M. Campillo, Space-Time Monitoring of Groundwater Fluctuations with Passive Seismic Interferometry. *Nature Communications* **13** (1), 4643 (2022), doi:10.1038/s41467-022-32194-3.

33. C.-W. Chen, L.-W. Wei, R. Yamada, T. Iida, Spatial Distribution of Landslides Triggered by the 2022 Taitung Earthquakes in Relation to Active Fault Systems, Topographic Effects, and Geological Conditions. *Geomorphology* **473**, 109615 (2025), doi:10.1016/j.geomorph.2025.109615.

34. O. Marc, N. Hovius, P. Meunier, T. Gorum, T. Uchida, A Seismologically Consistent Expression for the Total Area and Volume of Earthquake-Triggered Landsliding. *Journal of Geophysical Research: Earth Surface* **121** (4), 640–663 (2016), doi:10.1002/2015JF003732.

35. G.-W. Lin, *et al.*, Effects of Earthquake and Cyclone Sequencing on Landsliding and Fluvial Sediment Transfer in a Mountain Catchment. *Earth Surface Processes and Landforms* **33** (9), 1354–1373 (2008), doi:10.1002/esp.1716.

36. O. Marc, N. Hovius, P. Meunier, T. Uchida, S. Hayashi, Transient Changes of Landslide Rates after Earthquakes. *Geology* **43** (10), 883–886 (2015), doi:10.1130/G36961.1.

37. P. Steer, *et al.*, Earthquake Statistics Changed by Typhoon-Driven Erosion. *Scientific Reports* **10** (1), 10899 (2020), doi:10.1038/s41598-020-67865-y.

38. S. J. Dadson, *et al.*, Earthquake-Triggered Increase in Sediment Delivery from an Active Mountain Belt. *Geology* **32** (8), 733–736 (2004), doi:10.1130/G20639.1.

39. B. J. Mahler, F. L. Lynch, Muddy Waters: Temporal Variation in Sediment Discharging from a Karst Spring. *Journal of Hydrology* **214** (1), 165–178 (1999), doi:10.1016/S0022-1694(98)00287-X.

40. M. Pronk, N. Goldscheider, J. Zopfi, F. Zwahlen, Percolation and Particle Transport in the Unsaturated Zone of a Karst Aquifer. *Groundwater* **47** (3), 361–369 (2009), doi:10.1111/j.1745-6584.2008.00509.x.

41. Y. Zhou, *et al.*, Suspended Sediment Pulses and Sediment-Discharge Relationships in Earthquake-Affected Rivers Along the Tibetan Plateau Margins. *Water Resources Research* **62** (4), e2025WR042351 (2026), doi:10.1029/2025WR042351.

42. D. R. Montgomery, M. Manga, Streamflow and Water Well Responses to Earthquakes. *Science* **300** (5628), 2047–2049 (2003), doi:10.1126/science.1082980.

43. W. L. Wang, *et al.*, Assessment of Damage in Mountain Tunnels Due to the Taiwan Chi-Chi Earthquake. *Tunnelling and Underground Space Technology* **16** (3), 133–150 (2001), doi:10.1016/S0886-7798(01)00047-5.

44. T. Candela, E. E. Brodsky, C. Marone, D. Elsworth, Laboratory Evidence for Particle Mobilization as a Mechanism for Permeability Enhancement via Dynamic Stressing. *Earth and Planetary Science Letters* **392**, 279–291 (2014), doi:10.1016/j.epsl.2014.02.025.

45. A. Trofimov, B. Drach, M. Kachanov, I. Sevostianov, Effect of a Partial Contact between the Crack Faces on Its Contribution to Overall Material Compliance and Resistivity. *International Journal of Solids and Structures* **108**, 289–297 (2017), doi:10.1016/j.ijsolstr.2016.12.028.

46. P. A. Witherspoon, J. S. Y. Wang, K. Iwai, J. E. Gale, Validity of Cubic Law for Fluid Flow in a Deformable Rock Fracture. *Water Resources Research* **16** (6), 1016–1024 (1980), doi:10.1029/WR016i006p01016.

47. G. G. Meyer, N. Brantut, T. M. Mitchell, P. G. Meredith, O. Plümper, Time Dependent Mechanical Crack Closure as a Potential Rapid Source of Post-Seismic Wave Speed Recovery: Insights From Experiments in Carrara Marble. *Journal of Geophysical Research: Solid Earth* **126** (4), e2020JB021301 (2021), doi:10.1029/2020JB021301.

48. C. Sens-Schönfelder, R. Snieder, X. Li, A Model for Nonlinear Elasticity in Rocks Based on Friction of Internal Interfaces and Contact Aging. *Geophysical Journal International* **216** (1), 319–331 (2019), doi:10.1093/gji/ggy414.

49. M. Asnar, *et al.*, Anisotropy Reveals Contact Sliding and Aging as a Cause of Post-Seismic Velocity Changes. *Nature Communications* **16** (1), 7587 (2025), doi:10.1038/s41467-025-62667-0.

50. M. Bouchon, C. A. Schultz, M. N. Toksöz, Effect of Three-Dimensional Topography on Seismic Motion. *Journal of Geophysical Research: Solid Earth* **101** (B3), 5835–5846 (1996), doi:10.1029/95JB02629.

51. S. E. Hough, *et al.*, Localized Damage Caused by Topographic Amplification during the 2010 M 7.0 Haiti Earthquake. *Nature Geoscience* **3** (11), 778–782 (2010), doi:10.1038/ngeo988.

52. S.-J. Lee, Y.-C. Chan, D. Komatitsch, B.-S. Huang, J. Tromp, Effects of Realistic Surface Topography on Seismic Ground Motion in the Yangminshan Region of Taiwan Based Upon the Spectral-Element Method and LiDAR DTM. *Bulletin of the Seismological Society of America* **99** (2A), 681–693 (2009), doi:10.1785/0120080264.

53. L. Illien, *et al.*, Seismic Velocity Recovery in the Subsurface: Transient Damage and Groundwater Drainage Following the 2015 Gorkha Earthquake, Nepal. *Journal of Geophysical Research: Solid Earth* **127** (2), e2021JB023402 (2022), doi:10.1029/2021JB023402.

54. T. Clements, M. A. Denolle, The Seismic Signature of California's Earthquakes, Droughts, and Floods. *Journal of Geophysical Research: Solid Earth* **128** (1), e2022JB025553 (2023), doi:10.1029/2022JB025553.

55. P. Makus, M. A. Denolle, C. Sens-Schönfelder, M. Köpfli, F. Tilmann, Analyzing Volcanic, Tectonic, and Environmental Influences on the Seismic Velocity from 25 Years of Data at

Mount St. Helens. *Seismological Research Letters* **95** (5), 2674–2688 (2024), doi:10.1785/0220240088.

56. M. Kagabu, K. Ide, T. Hosono, K. Nakagawa, J. Shimada, Describing Coseismic Groundwater Level Rise Using Tank Model in Volcanic Aquifers, Kumamoto, Southern Japan. *Journal of Hydrology* **582**, 124464 (2020), doi:10.1016/j.jhydrol.2019.124464.

57. J. Jeanpert, *et al.*, Fracture Controlled Permeability of Ultramafic Basement Aquifers. Inferences from the Koniambo Massif, New Caledonia. *Engineering Geology* **256**, 67–83 (2019), doi:10.1016/j.enggeo.2019.05.006.

58. J. Rodriguez, S. Ustin, S. Sandoval-Solis, A. T. O'Geen, Food, Water, and Fault Lines: Remote Sensing Opportunities for Earthquake-Response Management of Agricultural Water. *Science of The Total Environment* **565**, 1020–1027 (2016), doi:10.1016/j.scitotenv.2016.05.146.

59. S. Gao, *et al.*, Shifts of Forest Resilience after Seismic Disturbances in Tectonically Active Regions. *Nature Geoscience* **17** (3), 189–196 (2024), doi:10.1038/s41561-024-01380-x.

60. J. Zhang, *et al.*, Eco-Hydrological Recovery Following Large Vegetation Disturbances from a Mega Earthquake on the Eastern Tibetan Plateau. *Journal of Hydrology* **651**, 132595 (2025), doi:10.1016/j.jhydrol.2024.132595.

61. T. Hosono, C. Yamada, M. Manga, C.-Y. Wang, M. Tanimizu, Stable Isotopes Show That Earthquakes Enhance Permeability and Release Water from Mountains. *Nature Communications* **11** (1), 2776 (2020), doi:10.1038/s41467-020-16604-y.

62. C.-Y. Wang, M.-L. Doan, L. Xue, A. J. Barbour, Tidal Response of Groundwater in a Leaky Aquifer—Application to Oklahoma. *Water Resources Research* **54** (10), 8019–8033 (2018), doi:10.1029/2018WR022793.

63. R. I. Acworth, L. J. S. Halloran, G. C. Rau, M. O. Cuthbert, T. L. Bernardi, An Objective Frequency Domain Method for Quantifying Confined Aquifer Compressible Storage Using Earth and Atmospheric Tides. *Geophysical Research Letters* **43** (22), 11,671–11,678 (2016), doi:10.1002/2016GL071328.

64. S. P. Neuman, P. A. Witherspoon, Theory of Flow in a Confined Two Aquifer System. *Water Resources Research* **5** (4), 803–816 (1969), doi:10.1029/WR005i004p00803.

65. P. Makus, C. Sens-Schönfelder, SeisMIC - an Open Source Python Toolset to Compute Velocity Changes from Ambient Seismic Noise. *Seismica* **3** (1) (2024), doi:10.26443/seismica.v3i1.1099.

66. G. D. Bensen, *et al.*, Processing Seismic Ambient Noise Data to Obtain Reliable Broad-Band Surface Wave Dispersion Measurements. *Geophysical Journal International* **169** (3), 1239–1260 (2007), doi:10.1111/j.1365-246X.2007.03374.x.

67. P. Makus, *et al.*, Deciphering the Whisper of Volcanoes: Monitoring Velocity Changes at Kamchatka's Klyuchevskoy Group With Fluctuating Noise Fields. *Journal of Geophysical Research: Solid Earth* **128** (4), e2022JB025738 (2023), doi:10.1029/2022JB025738.

68. P. Virtanen, *et al.*, SciPy 1.0: Fundamental Algorithms for Scientific Computing in Python. *Nature Methods* **17** (3), 261–272 (2020), doi:10.1038/s41592-019-0686-2.

69. J. M. Turowski, *et al.*, Taiwan Multi-Parametric Environmental Seismic Network (2022), doi:10.14470/GD993669.

70. J. Quinteros, *et al.*, The GEOFON Program in 2020. *Seismological Research Letters* **92** (3), 1610–1622 (2021), doi:10.1785/0220200415.

71. B. Rabus, M. Eineder, A. Roth, R. Bamler, The Shuttle Radar Topography Mission—a New Class of Digital Elevation Models Acquired by Spaceborne Radar. *ISPRS Journal of Photogrammetry and Remote Sensing* **57** (4), 241–262 (2003), doi:10.1016/S0924-2716(02)00124-7.

72. G. Ekström, M. Nettles, A. M. Dziewoński, The Global CMT Project 2004–2010: Centroid-Moment Tensors for 13,017 Earthquakes. *Physics of the Earth and Planetary Interiors* **200–201**, 1–9 (2012), doi:10.1016/j.pepi.2012.04.002.

73. G. C. Rau, T. Eulenfeld, C. Miller, Hydrogeoscience/Pygtide: PyGTide v0.9.1 (2026), doi:10.5281/zenodo.21483314.

74. L. Uieda, *et al.*, PyGMT: A Python Interface for the Generic Mapping Tools (2021), doi: 10.5281/ZENODO.4522136.

75. C. R. Harris, *et al.*, Array Programming with NumPy. *Nature* **585** (7825), 357–362 (2020), doi:10.1038/s41586-020-2649-2.

76. J. D. Hunter, Matplotlib: A 2D Graphics Environment. *Computing in Science & Engineering* **9** (03), 90–95 (2007), doi:10.1109/MCSE.2007.55.

Acknowledgments

We thank Christoff Andermann for discussions. We thank the Geological Survey and Mining Management Agency for providing the groundwater data.

Funding: N.B. was funded by the European Research Council under the European Union's Horizon 2020 research and innovation programme (project RockDeath, Grant agreement 101088963 to N.B.). The Taroko Earth Surface Observatory (TESO) is funded by the GFZ Helmholtz Centre for Geosciences.

Author contributions: Conceptualization: P.M., N.B., L.I., N.H. Data curation: P.M., W.-A.C., J.-M.C. Formal analysis: P.M., L.I. Investigation: J.M.T., W.-S.C., J.-M.C., W.-A.C., W.-Y.C. Methodology: P.M., N.B., L.I. Software: P.M. Supervision: N.H., J.M.T. Visualization: P.M. Writing – original draft: P.M. Writing – review & editing: P.M., J.M.T., N.B., N.H., L.I.

Competing interests: The authors declare that they have no competing interests.

Data and materials availability: The seismic data from the TQ network (*69*) used to compute the seismic velocity change time series can be downloaded from the Geofon FDSN service (*70*). Piezometric water levels for the wells are openly available with a one-day-sample interval from the Taiwan hydrogeological information system at `https://hydro.geologycloud.tw/`. The 10-minute-sampled piezometric data is provided as electronic supplement to this manuscript. The barometric and precipitation data for weather station C0T820 were obtained from Taiwan's

Central Weather Administration (CWA) at `https://codis.cwa.gov.tw`. To compute the PGA, we obtained data from stations F072 and F026 from the Taiwan Strong Motion Instrumentation Program (TSMIP) network, provided by the CWA at `https://gdms.cwa.gov.tw`. The digital elevation model used in the map plots was obtained from the Shuttle Radar Topography Mission (*71*). Locations of rivers and streams shown in Fig. 1 are copyrighted by OpenStreetMap contributors and available from `https://www.openstreetmap.org`, while we obtained the moment tensors from the global CMT project (*72*) at `www.globalcmt.org`. During peer-review: The research codes and raw data required to reproduce this work are included in the submission. Upon acceptance, these will be made available to the public via a DOI-minted archive (Zenodo). We computed the solid Earth tide predictions using the PyGTide software (*73*). Seismic velocity changes were estimated using the SeisMIC software suite (*65*). We plotted maps with PyGMT (*74*). Moreover, we heavily relied on the Python community packages NumPy (*75*), SciPy (*68*), and Matplotlib (*76*).

Supplementary materials

Supplementary Text

Figs. S1 to S7

Table S1

Supplementary Materials for

Typhoons reseal mountain groundwater systems after earthquake damage

Peter Makus *et al.*

*Corresponding author. Email: makus@gfz.de

This PDF file includes:

Supplementary Text
Figs. S1 to S7
Table S1

Supplementary Text

Taroko's aquifers

All four boreholes, from which we obtain data, are drilled into fractured metamorphic bedrock typical of eastern Taiwan. However, their hydraulic properties vary substantially, impacting their water level dynamics and suitability for tidal analysis. EHW-03 and EH-04 are drilled through unconfined aquifers hosted in marble and gneiss, respectively, with high transmissivities that lead to rapid recharge, apparent in their raw water level records (see Fig. 2 in the main text). Their tidal transfer functions yield poorly constrained phase estimates, precluding a tidal inversion. EH-04 is located adjacent to the Liwu River and, due to its high hydraulic conductivity, its piezometric water level closely tracks river stage, explaining the absence of persistent postseismic water level anomalies at this well. EHW-01 is confined within a low-permeability schist ($T \approx 1 \times 10^{-8}\,\mathrm{m}^2/\mathrm{s}$). Its transmissivity is so low that diffusion within the aquifer is slower than a half-period of the semi-diurnal tide, yielding no exploitable tidal signal. EHW-02 samples a semi-confined fractured aquifer isolated from the surface by $\sim$17 m of colluvium. Its intermediate transmissivity, $\sim 1 \times 10^{-6}\,\mathrm{m}^2/\mathrm{s}$, allows pore pressure diffusion within the tidal period while confinement suppresses atmospheric noise, making it the only well suited for our tidal inversion.

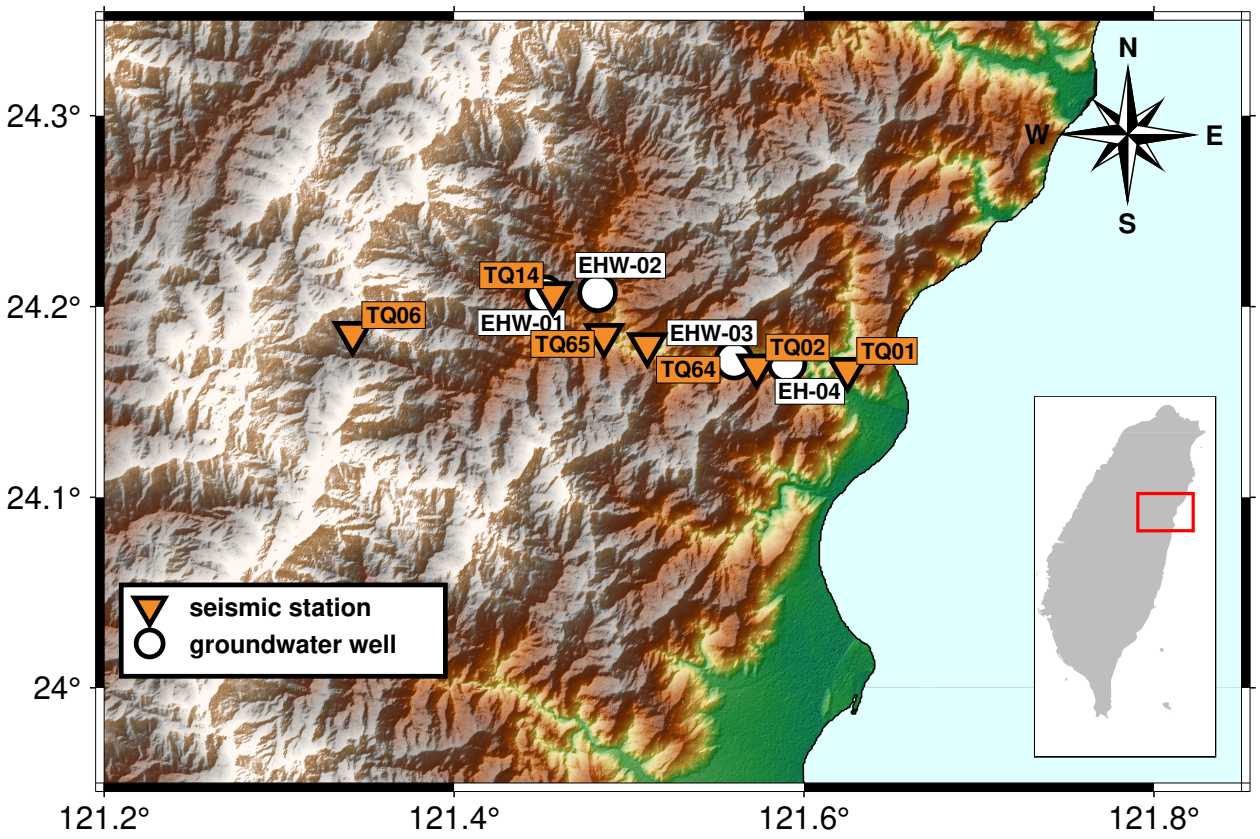


Fig. S1. Location and code of seismic stations and groundwater wells used in this work.

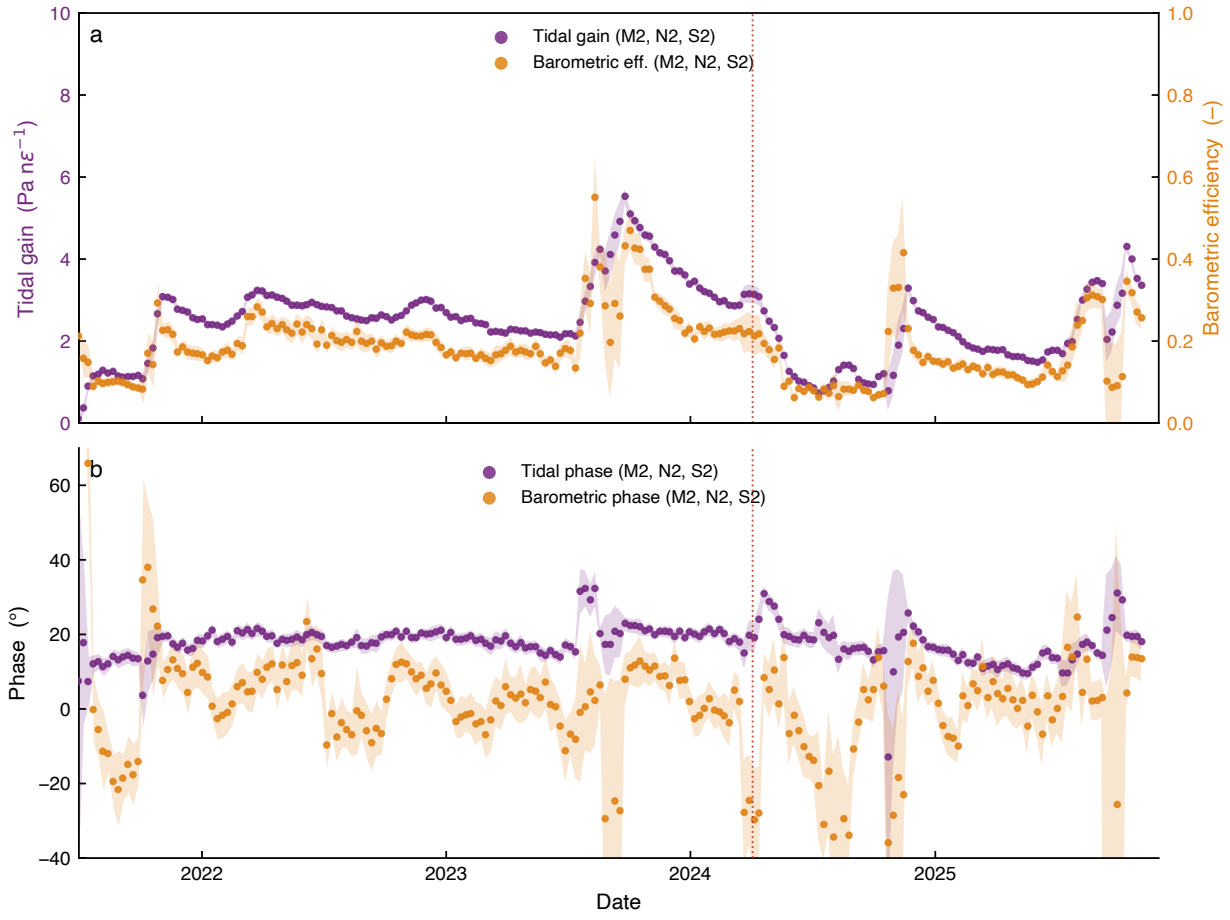


Fig. S2. Tidal and barometric transfer functions. The first part of the transmissivity inversion yields tidal and barometric gain (**a**) and phase (**b**) as a function of time. Both show a dependency on the groundwater level; this dependency is particularly apparent for the gain. The dashed red vertical line demarcates the M7.2 2024 Hualien earthquake.

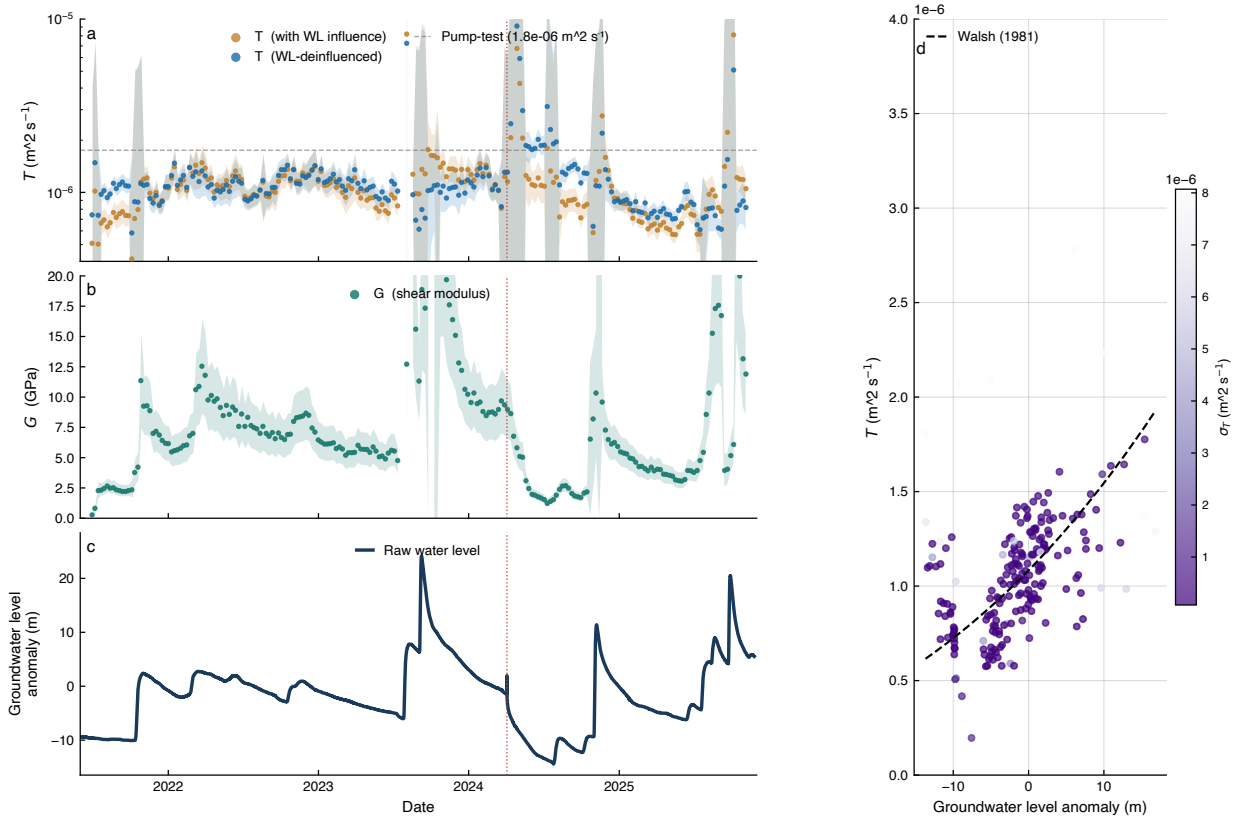


Fig. S3. Time-dependent transmissivity and shear modulus. The second part of the transmissivity inversion yields the aquifer's transmissivity $T(t)$ (**a**) and shear modulus $G(t)$ (**b**). Due to its strong water level dependency (shown in **c**), we do not interpret $G(t)$. In panel **a**, we compare T retrieved from hydraulic pump tests with the pore-pressure-corrected transmissivity. The dashed red vertical line demarcates the M7.2 2024 Hualien earthquake. Panel **c** shows the transmissivity as a function of the groundwater level anomaly up to the Hualien earthquake, with the best-fit curve for Eq. 5 derived from (*28*) superimposed as a yellow dashed line. The points are shaded according to their standard deviation.

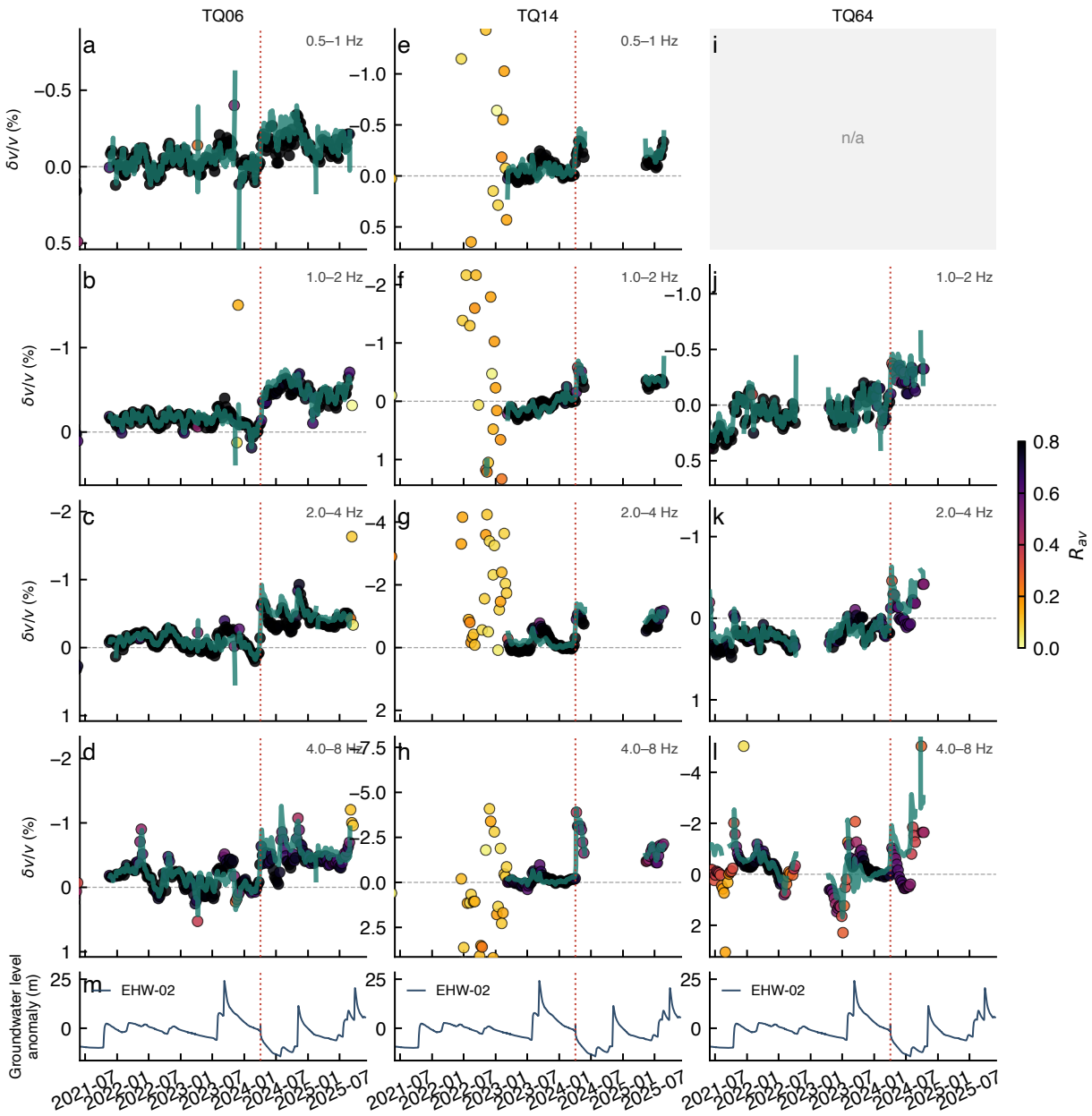


Fig. S4. Pore pressure correction of $\delta v/v$. We show $\delta v/v$ computed from the frequency bands and stations indicated in each panel. The pore-pressure-corrected $(\delta v/v)_{corr}$ is plotted in green, whereas the raw $\delta v/v$ is shown as a scatter plot with its colour depending on the average cross-correlation R_{av} as a quality metric. Note that lower frequency bands show lower pore pressure dependency. The performance of the pore-pressure correction varies from station to station. Panels marked with "n/a" are $\delta v/v$ time series that did not pass the quality control criteria.

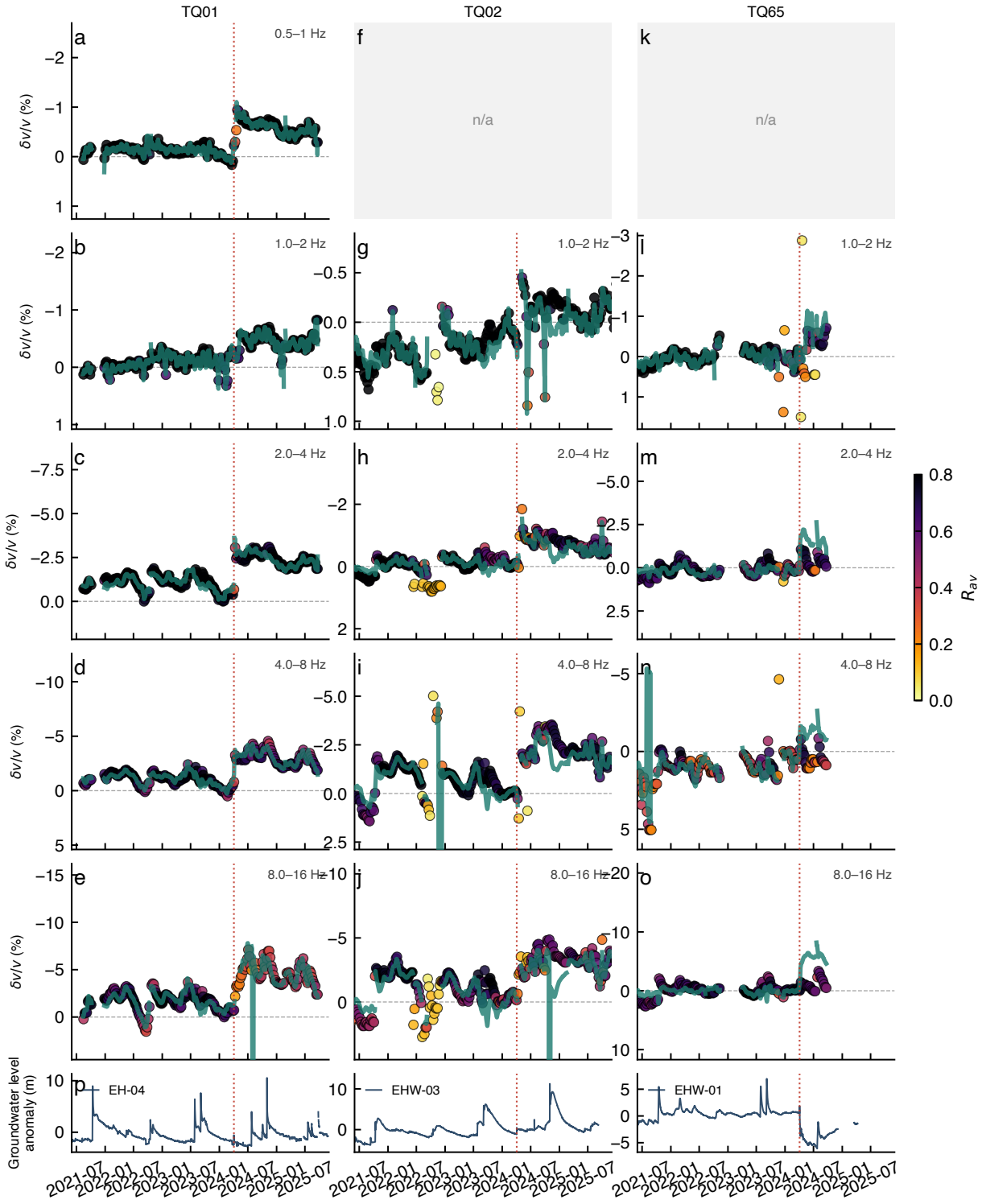


Fig. S5. Pore pressure correction of $\delta v/v$. Refer to Fig. S4's caption.

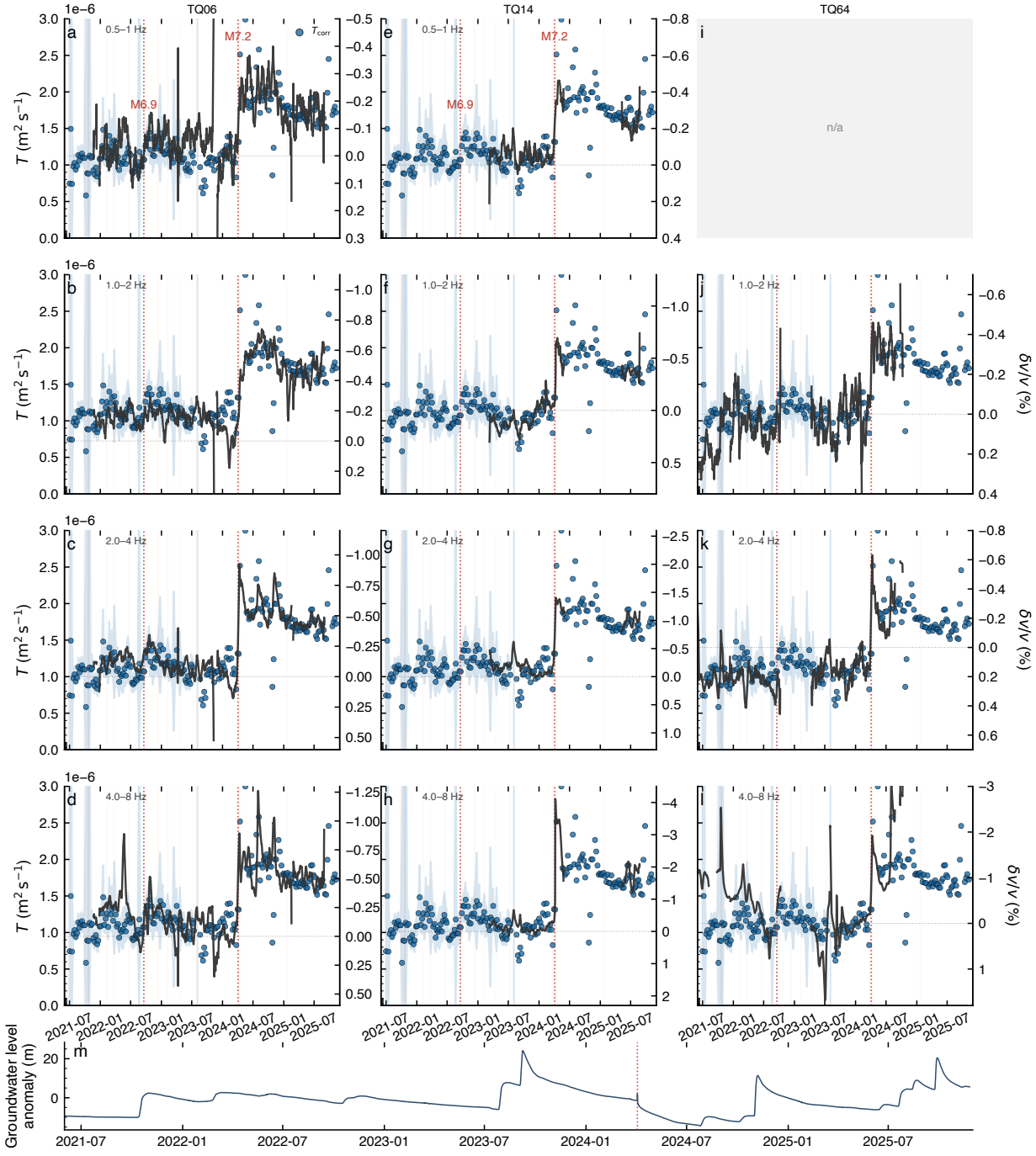


Fig. S6. Co-evolution of the transmissivity and the seismic wavespeed change ($\delta v/v$). We show the pore-pressure- and typhoon-corrected transmissivity (blue circles) against $\delta v/v$ (black solid curve) computed from the frequency bands and stations indicated in each panel. Panels marked with "n/a" are $\delta v/v$ time series that did not pass the quality control criteria. Note that lower frequencies show a clear covariance between $-\delta v/v$ and T. Origin times of the 2022 Taitung and 2024 Hualien earthquakes are indicated by red dotted lines. Panel p shows the piezometric record of EHW-02.

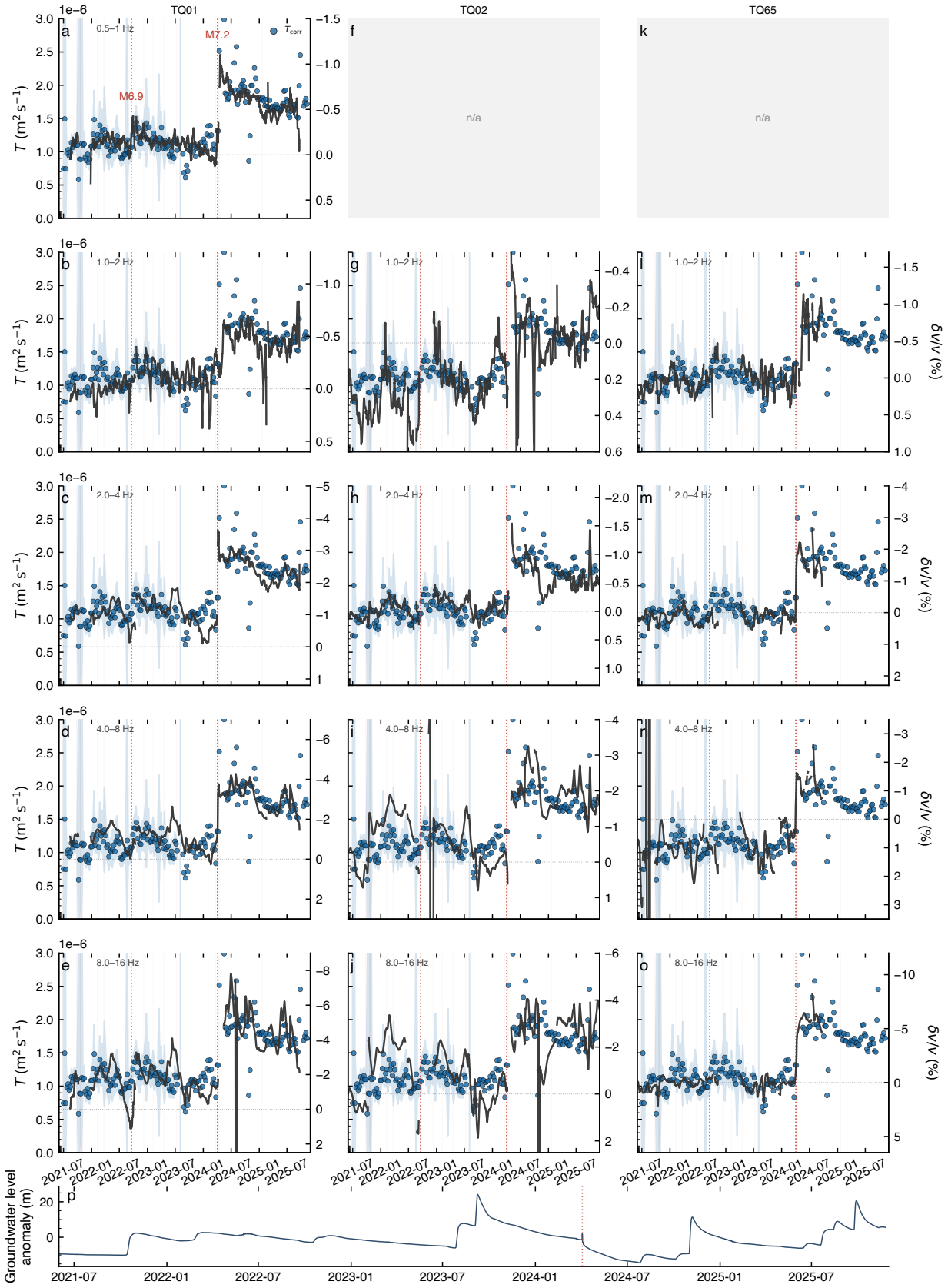


Fig. S7. Co-evolution of the transmissivity and the seismic wavespeed change ($\delta v/v$). Refer to Fig. S6's caption.

Table S1. Hydraulic pump test results for borehole EHW-02. We use the storativity values to parametrise the transmissivity inversion, whereas the hydraulic conductivity K serves purely as a validation metric.

$z_{\min}$ (m)	$z_{\max}$ (m)	K ($\mathrm{m\,s^{-1}}$)	S	S_s ($\mathrm{m^{-1}}$)
5.00	10.00	4.50×10^{-6}	–	–
11.00	16.00	2.80×10^{-5}	–	–
30.00	31.50	2.70×10^{-8}	1.70×10^{-5}	1.10×10^{-5}
39.00	40.50	2.90×10^{-8}	2.20×10^{-4}	1.40×10^{-4}
52.50	54.00	2.20×10^{-8}	4.20×10^{-4}	2.80×10^{-4}
54.00	100.00	4.00×10^{-7}	4.60×10^{-5}	1.00×10^{-6}
60.00	100.00	6.10×10^{-8}	4.00×10^{-5}	1.00×10^{-6}
64.40	65.90	2.80×10^{-8}	1.10×10^{-3}	7.40×10^{-4}
71.80	73.30	6.70×10^{-8}	2.00×10^{-4}	1.40×10^{-4}
87.00	100.00	1.30×10^{-7}	1.30×10^{-5}	1.00×10^{-6}
87.00	88.50	4.40×10^{-7}	1.90×10^{-6}	1.30×10^{-6}
28.00	100.00	3.10×10^{-6}	7.20×10^{-5}	1.00×10^{-6}